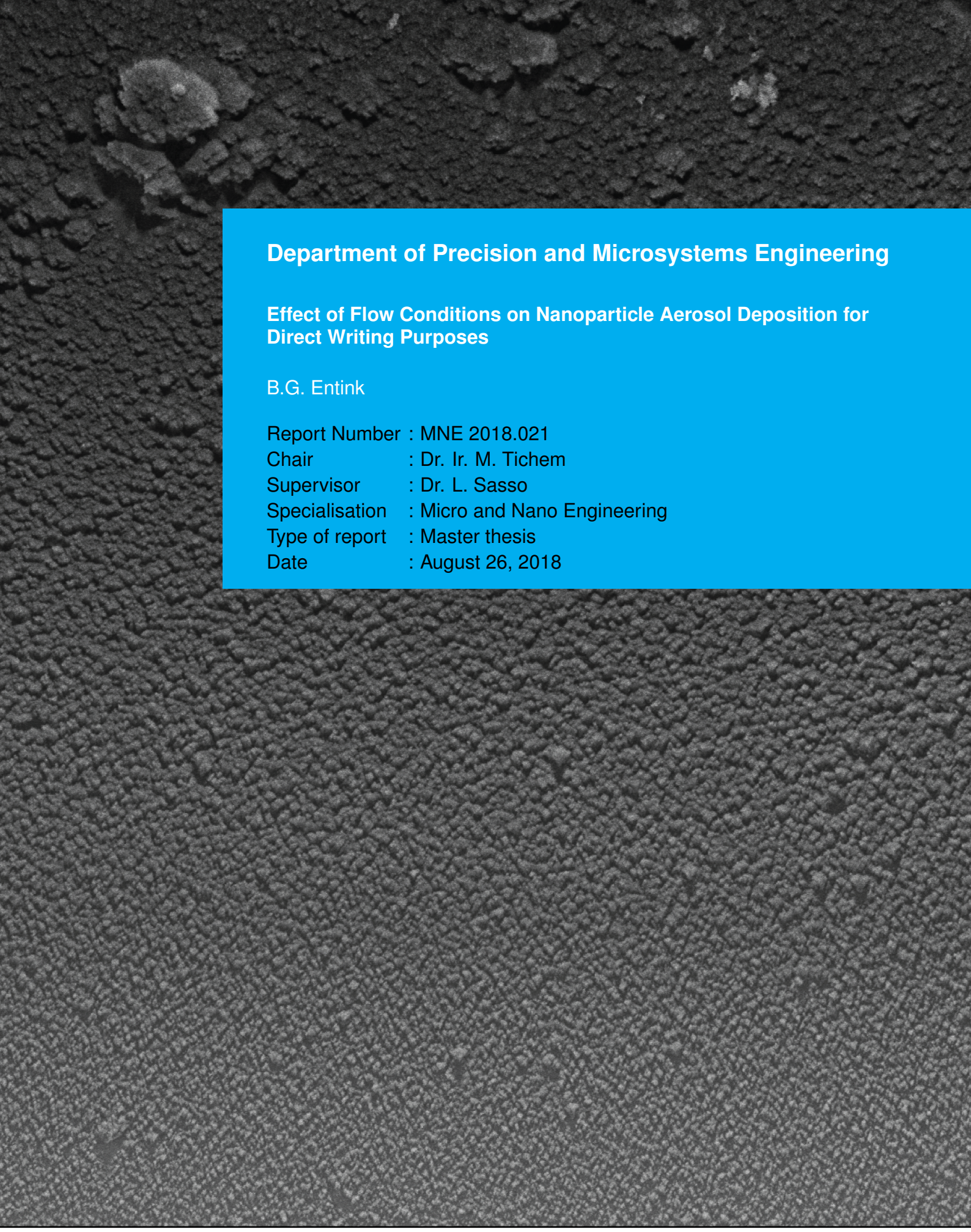

Department of Precision and Microsystems Engineering

Effect of Flow Conditions on Nanoparticle Aerosol Deposition for Direct Writing Purposes

B.G. Entink

Report Number : MNE 2018.021
Chair : Dr. Ir. M. Tichem
Supervisor : Dr. L. Sasso
Specialisation : Micro and Nano Engineering
Type of report : Master thesis
Date : August 26, 2018

TU Delft Delft University of Technology

Challenge the future

Effect of Flow Conditions on Nanoparticle Aerosol Deposition for Direct Writing Purposes

by

B.G. Entink

to obtain the degree of Master of Science
at the Delft University of Technology,
to be defended publicly on Thursday September 13, 2018.

Student number:	4509633	
Project duration:	September 1, 2017 – September 13, 2018	
Thesis committee:	Dr. Ir. M . Tichem,	TU Delft, chair
	Dr. L. Sasso,	TU Delft, supervisor
	S. Aghajani, MSc,	TU Delft
	Dr. D.S.W. Tam	TU Delft

This thesis is confidential and cannot be made public.

An electronic version of this thesis is available at `http://repository.tudelft.nl/`.

TU Delft

Abstract

Nanoparticles have unique properties that are sought after for the development and improvement of applications. Prerequisite to achieve these applications, methods are required to put the nanoparticles in different patterns and arrangement on a target substrate.

In the course of developing an aerosol-based nanoparticle printing system, this work explores the results of different aerosol deposition configurations.

The work is based on a spark ablation process that generates an aerosol of argon and copper nanoparticle agglomerates. The deposition configuration deposits the aerosol on a target substrate. Three configurations are explored, one which deposits at subsonic velocities, and two which deposit at sonic velocities. The aim is to find the most favourable deposition conditions for the direct writing of nanoparticle patterns.

It is found that a sonic deposition configuration with a low pressure ratio at small substrate distances has the smallest deposit diameter. The configuration allows for the patterning of narrow lines, that consist of two deposition regions: a micro-aggregate region and a nanoparticle region. It was found that the density of these regions is mainly influenced by the process variables of the spark ablation process, and can thus be used to gain a high consistency and well-defined edges.

Preface

This thesis is the result of a project that explored the capabilities of a new set-up. The opportunity was given to me by Marcel Tichem and Luigi Sasso, who also supported me throughout the project, for this I am thankful. In addition, thank you Saleh Aghajani for helping out in the project and making me rethink several aspects of the thesis.

The set-up had some initial problems, which turned out to be of great help in gaining an understanding of the system. For the invaluable help in fixing these problems, and many more things, I would like to thank Harry Jansen and Patrick van Holst.

Some of the experiments were performed on location at VSP. I would like to thank the people at VSP for providing the help for the experiments.

Of course this thesis would have never been written without the support of my friends and family. Thank you all.

B.G. Entink
Delft, August 26, 2018

Contents

1

Introduction

Nanotechnology applications utilising nanoparticles are of an increasing interest in a large variety of research fields. Nanoparticles have dimensions below 100 nm and as a result show unique properties and effects. Surprisingly, nanoparticle technologies are already found all around us, for example in medicinal drug delivery, car coatings, and even in food products [1]. The increase in attention is supported by the further development of methods used for nanoparticle characterisation and fabrication. Specifically the improvements on control, in both handling and synthesis, of smaller dimensions allows for faster discovery of new applications.

Currently, the goal is to gain the ability to control the smallest of particles and pattern these in any desired shape. One of those future visions is depicted in Figure 1.1, which illustrates a hypothetical manufacturing line with two aerodynamic lenses that 3D prints with nanoparticles [2]. However, the achievement of this stage requires a large amount of further research. In addition to research on achieving more knowledge on nanoparticles and their potential applications, research should also aim to further investigate bringing the fabrication processes to manufacturing lines.

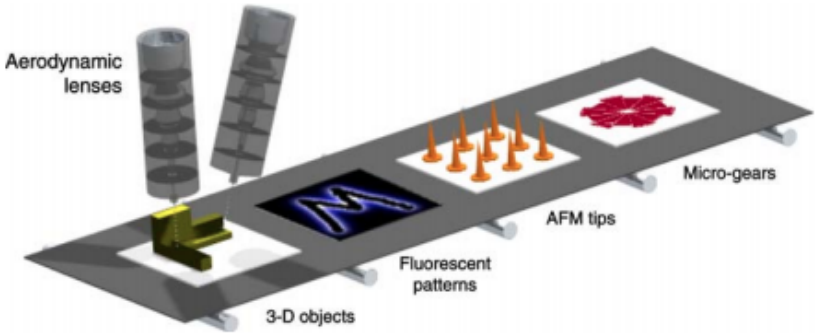

Figure 1.1: A hypothetical manufacturing line that prints patterns and 3D objects with aerodynamic lenses that focus nanoparticles [2].

1.1. Direct writing of nanoparticles

Research on nanoparticle applications often requires the nanoparticles in patterns or deposited as a thin film. Patterns are for example used in conductive lines [3], while thin films are more often used as coatings [2], but also gas sensing [4]. The small dimensions of nanoparticles introduce new functionalities and properties, mostly due to their high surface to volume ratio and quantum physics. Additional information on the effects of nanoparticles is given in Appendix A. Table 1.1 gives a non-exhaustive list of research on nanoparticle applications and shows the diverse possibilities. However, the processes, for both nanoparticle synthesis and nanoparticle handling, are often limited to lab environments. Additionally, different requirements for the functionalities demand a versatile and high level of control over the placement and particle size of the nanoparticles. To make these type of applications accessible to the consumer market, further research is re-

quired on scalable nanoparticle synthesis and nanoparticle deposition processes.

A promising field for deposition of patterns and thin films is that of direct writing, of which Figure 1.1 is a futuristic example. The definition of direct writing, given by [5], is the following: "Direct writing denotes a group of processes which are used to precisely deposit functional and/or structural materials on to a substrate in digitally defined locations". Direct writing contains a large amount of different technologies like: inkjet printing [6], two-photon-polymerisation [5], liquid extrusion [5], and aerosol deposition [7]. For the patterning of nanoparticles, inkjet printing requires the nanoparticle to be in the ink, a liquid suspension [6], while two-photon-polymerisation and liquid extrusion do not aim to deposit nanoparticles [5]. However, aerosol deposition (AD), as the name implies, deposits particles mixed in a gas. Though these particles can be small droplets [8], only nanoparticles are considered in this work . Contrary to inkjet printing, no additional process that could influence the deposit is required to remove the medium in which the nanoparticles reside, thus advantageous for the direct writing of different materials. This work explorers the direct writing process, aerosol deposition, as a scalable deposition method.

This section provides an introduction to two subsystems seen in similar systems: the nanoparticle synthesis and aerosol deposition. Both are of importance to gain the ability to precisely deposit the nanoparticles.

Table 1.1: A list of applications for which the use of nanoparticles is researched to improve on a certain aspect. The table includes the research goal for the application, the property which is utilized and the materials used in the references.

Applications	Research goal	Functionality	Used material	References
Solar panels	To decrease the size of solar generators.	Photovoltaic	CdSe, InP	[9, 10]
	To increase the absorption of incident light.	Surface plasmon resonance	Ag	[11]
	To research the possibilities of luminescent solar concentrators.	Luminescence	CdSe, CdS	[12]
Smart textiles, High strain environments	To remove the external power supply for electronics.	Piezoelectricity	$Pb[Zr_xTi_{1-x}]O_3$, $FAPbBr_3$	[13–15]
Nanogenerators	To generate electricity from strain.	Piezoelectricity	$FAPbBr_3$, ZnO	[16]
	To generate electricity from friction.	Triboelectricity	SiO_2, $SrTiO_3$	[17–19]
	To generate electricity from temperature fluctuations.	Pyroelectricity	ZnO	[20]
Construction, Textiles, Electronics	To increase the material strength by nanoparticle addition.		SiC	[21, 22]
	To make materials heat resistant.	Heat conductivity		[22]
	To add conductivity to non-conductive materials.	Electrical conductivity	Ag	[23]
Gas sensors	To make gas sensing films.	Diffusivity	WO_3	[4]
Electronic chips	To pattern particles on the nanoscale.	Electrical conductivity	Cu	[3]
Medical equipment	To increase bacterial resistance.		TiO_2	[24]
Construction	To create an anti reflective layer.	Index of refraction	SiO_2, CeO_2	[25]
	To add a layer which is flame retardant.	Environmental stability	TiO_2	[26]
	To add a hydrophobic layer.	Surface roughness	SiO_2	[27]

1.1.1. Nanoparticle synthesis

The nanoparticles used in direct writing processes come in different forms and mediums. Two different methods of bringing nanoparticles into the system are distinguished.

- **Off-line synthesis**; the synthesis occurs at a different location and requires additional processes to make the nanoparticles available for transport and storage. The particles are often provided in a liquid or in a powder form. Synthesis processes include high-energy milling [28].
- **On-line synthesis**; the synthesis occurs close to the deposition. Synthesis processes include pulsed laser ablation [29] and spark ablation [30].

This work utilises the spark ablation process due to the on-line synthesis capabilities, and the other advantages discussed in the next section, The spark ablation process is schematically given in Figure 1.2. A high voltage spark is generated between the two electrodes, indicated by *1*. The RC-circuit controls the frequency at which these sparks occur. Each spark ablates, otherwise denoted as vaporises, some of the electrode material. The vaporised material is transported away from the electrodes by a carrier gas. The transport results in a quick reduction in gas temperature and as a result the vaporised material coalesces into primary nanoparticles (*2*). After the vapour phase, the combination of particles and the carrier gas is considered an aerosol. When the energy is reduced to the point where coalescence cannot occur, the primary nanoparticles start to agglomerate due to collisions, shown by *3*.

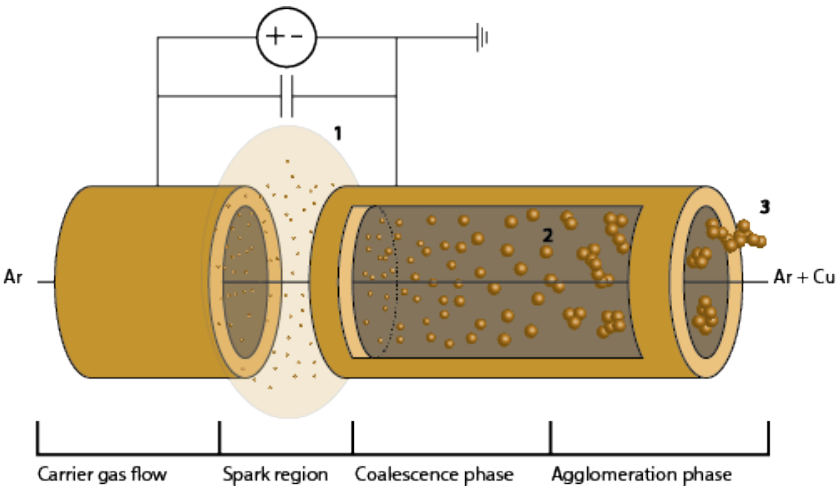

Figure 1.2: Schematic overview of the spark ablation process. A carrier gas flows towards the spark region where a material vapour cloud (1) is generated by high voltage sparks. The flow transports and quenches the evaporated material, which results in coalescence of the vapour cloud into primary nanoparticles (2). After the critical size, the particles start to agglomerate (3).

To prevent ambiguities in the naming of particles, Figure 1.3 illustrates four main hierarchies that are considered of importance for this and future work. The atomic structure of a particle (*1*) affects the properties and functionalities of the material. The material is in amorphous state when no order is present in the atomic structure. When the atomic structure is ordered, the material has a crystal structure defined by a repetitive building block, the unit cell. In total, 32 crystal types exist, identifiable by this unit cell and the interconnection between other, similar unit cells [31].

The primary nanoparticle (*2*) is the particle that nucleates and grows from the vapour phase a single coherent unit. The agglomerate of nanoparticles consists out of clustered primary nanoparticles, which results in a larger particle with boundaries between the atomic structures (*3*). The amalgamate of nanoparticles (*4*) shows similarities with the agglomerate. However, the connection between primary nanoparticles shows differences; No boundaries appear in the amalgamate due to fusion of primary nanoparticles.

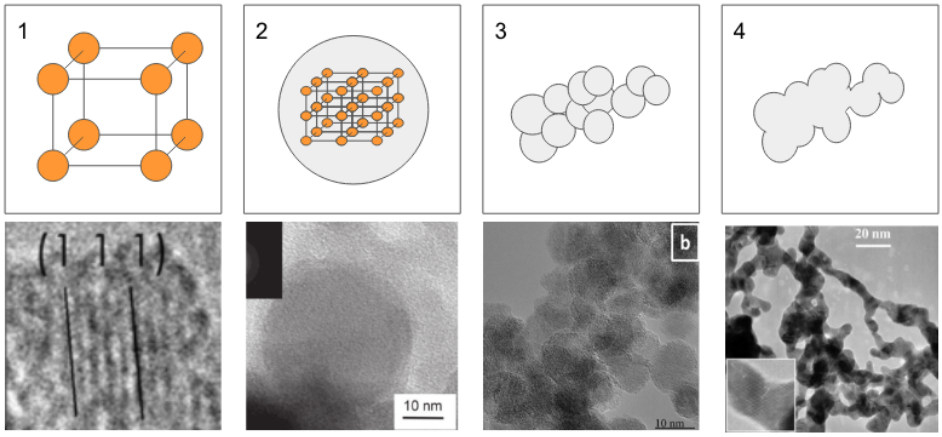

Figure 1.3: Schematic overview and examples of the four hierarchy levels considered of importance to this and future work. 1) Atomic structure of the nanoparticles. The example, taken from [32], illustrates the atomic structure of a silicon primary particle imaged by a HRTEM. The lines visualize the orientation of the atomic structure. 2) A primary nanoparticle. The example, taken from [33], illustrates a germanium primary nanoparticle. 3) An agglomerate of nanoparticles which consists out of primary nanoparticles with clear boundaries between particles. The example, taken from [34], illustrates an agglomerate of $Si_{1-x}Ge_x$ nanoparticles. 4) An amalgamate of nanoparticles which consists out of primary nanoparticles without boundaries between particles. The example, taken from [35], illustrates an amalgamate of Au-Pd nanoparticles which are sintered at the boundaries, the inset shows that the sintered boundary forms a uniform internal atomic structure.

1.1.2. State of the art in spark ablation

Besides being a good option for on-line nanoparticle synthesis, the spark ablation process has more advantages of interest: the scalability, the material versatility and a narrow size distribution on the primary nanoparticles [36].

The work done by [37] shows the scalability of spark ablation, otherwise denoted as spark discharge. The research shows that the placement of several electrodes in parallel is a valid strategy for a higher synthesis rate. The main reason for this is the similar energy consumption per gram for both a single machine and multiple machines. It should be noted that the overall energy efficiency is low compared to the theoretical minimum. In this research this is attributed to the utilised thermal energy. Additionally, though no energy comparison is made, [38] shows that the particle concentration is proportionally increased with the amount of electrode pairs connected in series.

Literature shows the material versatility for the spark ablation process. For example [4] shows the synthesis of an oxide (WO_x) thin film, [33] shows the synthesis of semiconducting (Ge and Si) nanoparticles and [39] shows the synthesis of metallic nanoparticles (Pd, Pt, Au and Ag).

The research of [39] paired the monometallic electrodes to synthesise alloys. However, the result was a mixture of monometallic nanoparticles. The mixture ratio depended on the electrode material and whether the electrode was placed as an anode(+) or cathode(-). Additionally, the vaporisation rate was dependent on the material and was attributed to the material dependent ionization potential. With an identical configuration [35] reported a similar mixture of monometallic nanoparticles. Alloyed electrodes were also tested and resulted in material ratios about the same to that of the alloyed electrode ratio.

The carrier gas influences the spark breakdown voltage [40] and the coalescence phase [41]. Noble gases are used to prevent chemical reactions with the electrode material. However, [42] showed that for silicon the addition of hydrogen increases the crystallinity of the deposit due to reduction of oxygen in the carrier gas. Additionally, the primary nanoparticles become passivated and are stopped from agglomerating. The carrier gas also has a direct influence on the deposition since the speed of sound differs per gas [43].

The size distribution of the nanoparticles generated with spark ablation have been thoroughly investigated [38]. The size distribution for the primary nanoparticles is relatively narrow, [38] reports standard deviations of less than $2nm$ on particles with a mean diameter between 10 and 50 nm. However, the ag-

glomeration of nanoparticle is uncontrolled and, as shown in [44], have a wider size distribution.

This shows that the spark ablation process is suitable for the synthesis of nanoparticles of a wide range of materials. In addition, the process allows for easy changes of various other variables like the spark variables, carrier gas and electrode combinations. However, the the final particle sizes are dependent on these variables and thus the deposition process is required to deposit aerosols with particles that have a wide size distribution.

1.1.3. Aerosol deposition

The deposition of aerosols is well researched for the applications of cold spray technology. Cold spray technology utilises high upstream pressures to accelerate the particles. However, due to the high drag at atmospheric pressure, the particles are required to be larger than those considered in this work [45]. Aerosol deposition is similar to cold spray methods but instead of deposition in atmospheric conditions it utilises a vacuum [46]. Specifically, this has implications for the velocities due to reduction of the drag force. This also means there are two ways to potentially improve on the deposition process: by increase of the velocity due to better flow development or further reduction of the drag force by a higher vacuum.

This research considers two methods of aerosol deposition, denoted as subsonic and sonic. Whether a flow becomes a subsonic or sonic jet after a restriction is dependent on the pressure ratio between the upstream pressure (p_1) and downstream pressure (p_2). Equation 1.1, where γ is the material dependent heat capacity ratio of the gas, gives the minimum downstream pressure (p^*) for subsonic flow.

$$\frac{p^*}{p_1} = \frac{2}{\gamma+1}^{\frac{\gamma}{\gamma-1}} \tag{1.1}$$

A subsonic flow ($p_2 > p^*$) accelerates or decelerates with a converging or diverging channel respectively. Figure 1.4a shows a schematic of the flow development through and after a subsonic nozzle. The jet diverges after the nozzle and in this process decelerates. When a substrate is placed in the free jet stream, as illustrated in Figure 1.4b, the subsonic jet creates a stagnation region at the substrate. In the stagnation region the flow lines start to split and go around the substrate.

The stagnation point is where the flow moves around and where the gas velocity is equal to zero. The size of the stagnation region depends on the gas velocity of the jet: for greater velocities, sharper flow bends occur and thus the stagnation region becomes smaller.

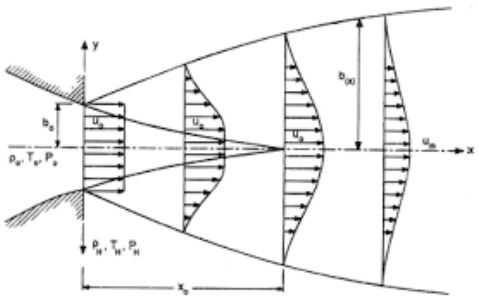

(a) Schematic of a free subsonic jet that illustrates the flow development [48].

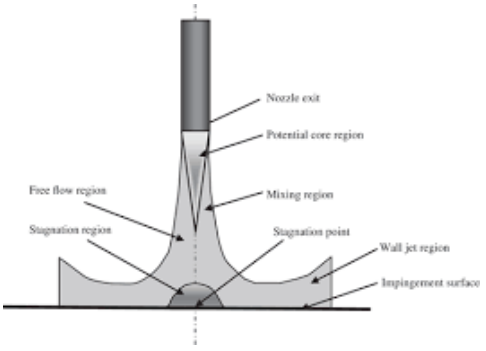

(b) Schematic on an impinged subsonic jet with the components indicated [49].

A sonic flow ($p_2 < p^*$) is the result of a restriction that reaches the limit of the flow (Q) passing through. The limit, when the flow is choked, means the gas velocity is equal to the speed of sound at the throat, in other words the Mach number is equal to unity. After the choked restriction, opposite to the effect of a diverging channel for subsonic flow, a divergence causes the Mach number to exceed unity and accelerate further into the sonic regime. Figure 1.5a shows a schematic of the flow development through and after a sonic restriction.

The gas expands rapidly due to the change in pressure and as a result accelerates. A pressure boundary forms on the sides of the jet as a result of the decrease in pressure in the jet and contains the expansion. As seen in the schematic, the jet stays focused throughout the flow development.

An important part of the flow expansion are the Mach disks. The first Mach disk generates at a distance L_m, as calculated by Equation 1.2[43] for which d_n is the throat diameter. The Mach disks continue, though weaker, with similar intervals until the flow loses too much energy and turns toward a subsonic jet.

Figure 1.5b shows a schematic of an impinged sonic jet. A bowshock is formed close to the substrate where the sonic flow compresses to the subsonic regime. Behind this bowshock, similar to an impinging subsonic jet, a stagnation area is formed. The flow parallel to the substrate, commonly referred to as the wall jets, can reach sonic velocities if the pressure ratio between the stagnation area and the surroundings is smaller than that given by Equation 1.1.

$$L_m = 0.67\, d_n \sqrt{\frac{p_1}{p_2}} \tag{1.2}$$

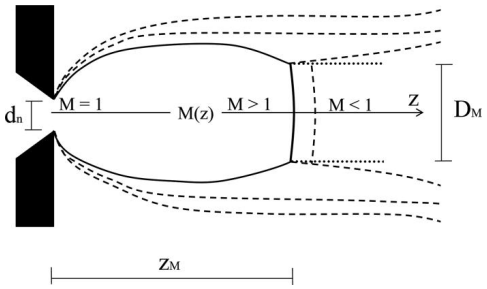

(a) Schematic of a free sonic jet that illustrates the flow development [47].

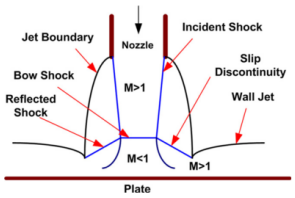

(b) Schematic on an impinged sonic jet with the components indicated [47].

Whether a particle impacts on the substrate is dependent on the dimensionless Stokes number. The number is a ratio of the particle relaxation time (τ_p) to the characteristic time of the flow (τ_f), as given in Equation 1.3. The Stokes number characterises the accuracy of a particle to stay attached to the flow lines. For Stokes values smaller than unity the particles follow the flow lines accurately while for values larger than unity they escape due to small disturbances in the flow lines [50]. Figure 1.6 shows a schematic of this behaviour.

$$Stk = \frac{\tau_p}{\tau_f} \tag{1.3}$$

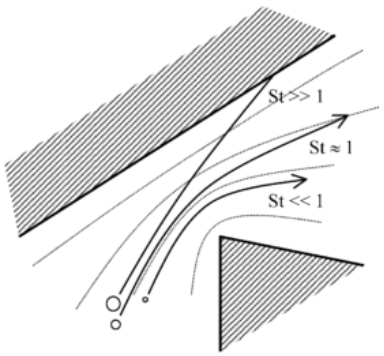

Figure 1.6: The behaviour of particles with different Stokes numbers. Particles with a Stokes number below follow the flow accurately, while for values above unity they escape the flow easily [51].

The time a particle takes to adjust to velocity changes is indicated by τ_p [8]. Nanoparticles have low values for t_p due to their relatively low mass, while τ_f tends to be proportional with the gas flow velocity and is

thus relatively high, specifically for sonic jets. Literature gives different equations for τ_p and τ_f depending on the flow parameters, notably the Reynolds number, the Mach number, the upstream to downstream pressure ratio, and the substrate distance to nozzle throat diameter ratio are of importance [52].

Correlations given for the Stokes number by [52], [47] and [53] include the Cunningham correction, which is introduced to account for the slip. The slip is a result of the gas mean free path being large in comparison with the characteristic dimension of the system, in this case the diameter of the nanoparticle agglomerates.

1.1.4. State of the art in aerosol deposition

Due to the relative simplicity of subsonic deposition configurations, a large amount of research aims to improve the focus of nanoparticles on the centreline of the jet. Two different approaches to gain a smaller deposition width can be categorised as: aerodynamic lens systems and sheath gas nozzles.

The research on aerodynamic lens systems shows that nanoparticles are focused by consecutive convergences, or so-called lenses [54–56]. The lens system modelled by [55] focuses sub-30 nm particles. Diffusion effects in the lens system limits the deposition of particles smaller than 5 nm. The lens system focuses the particles that are sized between 10 and 50 nm within a 1 mm deposit diameter with a nozzle (diameter of 2.42 mm). One thing to note is that large particles are more focused towards the centre line, introducing a radial particle size gradient. A similar study was undertaken by [56] and gives additional information on the pressure drops and gas velocities between lenses. The Stokes number increases after each lens due to the Cunningham slip correction factor dependence on the gas free mean path.

Instead of focusing the particles before the deposition, sheath gas nozzles push the aerosol jet towards the centreline after the nozzle. The work done by [57] and [58] show that higher sheath gas velocities influence the diameter of the deposits. The line width decreases below the diameter of the nozzle, which in comparison to an impinged subsonic jet (Figure 1.4a) is an interesting result.

Similarly, [51] reviewed the focusing of particles for sonic jets. Specifically of interest is the difference between deposition by a capillary or thin plate orifice. While for the capillary nozzle the particles focus on the centreline within the nozzle [59], the thin plate orifice focuses the particles after the nozzle [60]. The focusing effect for the thin plate orifice is dependent on particle size, with the focus point further away for small particles. In [61] a comparison is given for several nozzle designs for the collection of nanoparticles. The work concludes that the thick plate orifice performs better than a thin plate orifice. This is in agreement with research done on impactors, in which the goal is to filter particles above a certain size from an aerosol [52, 62]. Several works confirmed experimentally that smaller particles deposit at further substrate distances due to better flow development after the nozzles [47]. However, the impactor research aims to filter instead of focus the particles, and thus lacks information on deposition consistency, vital to this work.

1.2. Research goal

Currently, nanoparticle applications are limited by not yet scaled production methods. By the development of a system that is capable of controlling the nanoparticle amount, deposition location, and morphology; and in addition is employable in manufacturing lines, it is perceived that nanoparticle applications become more accessible to the consumer market.

The direct writing of aerosols shows potential for such a system. However, to adopt the system in manufacturing lines it requires the nanoparticle synthesis and the deposition to be scalable. In addition, to be able to produce applications with different requirements, the system needs to cope with different materials and substrates.

A scalable nanoparticle synthesis process is spark ablation, which generates an aerosol that consists of a carrier gas and agglomerates of nanoparticles. These nanoparticle agglomerates have a relatively wide particle size distribution and thus impose requirements on the deposition. Designs of nanoparticle deposition configurations generally aim to deposit a monodisperse aerosols. This means design reconsiderations are required for the deposition of an aerosol generated by spark ablation.

This research is the first step in the first steps are made with a new This research compares two types of flow for aerosol deposition, subsonic and sonic, which are commonly found for the deposition of monodisperse aerosols. The goal of the work is to find the most suitable deposition configuration for the writing of nanoparticle patterns, which as seen in other works, are mainly characterised by:

- Narrow lines; narrower lines allow for a more efficient substrate usage.
- Well-defined edges; the particle density gradient should decrease rapidly at the edges to prevent different nanoparticle behaviour on the edges.
- High consistency; the line should have similar thickness and morphology throughout the pattern.

The main research question of this work is:

'What are the most favourable deposition conditions for the direct writing of nanoparticle patterns?'

This question is split into two sub-questions:

1. What is the most suitable deposition configuration for direct writing?
2. What is the influence of the process variables on the deposition?

1.3. Project approach

This work uses a commercially available spark ablation apparatus for the synthesis of an aerosol. The aerosol that is generated is directly deposited in a vacuum chamber, for varying deposition conditions. The planning of the project is given with milestones and deliverables in Figure 1.7. By finishing the last milestone, it is expected that an answer is found to the research question.

The first part of the research aims to get the experimental set-up to a functioning level, which means nanoparticles are synthesised and deposited ($D1$). Due to the significant differences in the deposition configurations, it is expected that more work is required to make the set-up function for all configurations ($D2$). These two deliverables complete the first milestone ($M1$).

The second milestone aims to answer the first sub-question. First, single spot deposits with a variation in pressure and substrate distance are compared per configuration based on deposit shape, deposit diameter and deposit consistency. In this case the deposit consistency is determined by the particle density, particle sizes, and the radial dependence of both. This shows how each deposition configuration is influenced by vacuum pressure and substrate distance ($D3$). The configuration with the highest potential for the direct writing of nanoparticle patterns is determined by a combination of the deposit diameter, the deposit pattern and the

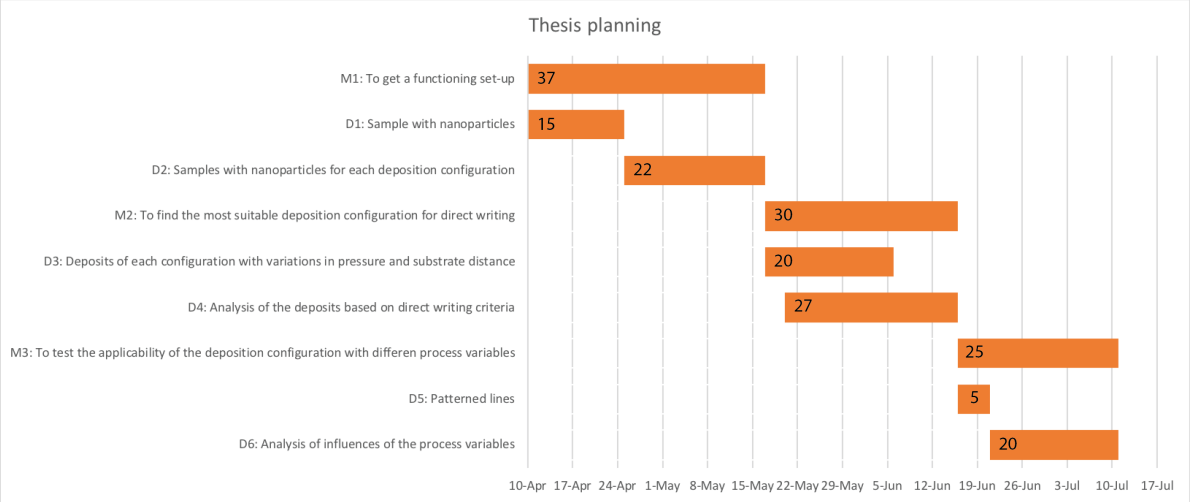

Figure 1.7: Project planning, milestones are indicated with M, deliverables are indicated with D. The numbers in each bar indicate the duration of the milestone/deliverable in days.

observability of nanoparticles. This is expected to give the most suitable deposition configuration ($D4$), and thus completes $M2$ with an answer to the first sub-question.

The third milestone tests the applicability of the found deposition configuration. The influence of the deposition variables, substrate distance and vacuum pressure is found in $M2$. The deposition configuration is used for the direct writing of lines with different flow rate, spark current, spark voltage, writing speed and writing sweeps ($D5$). The influence of these variables is then analysed by optical microscopy and electron microscopy to verify the viability of the configuration. The lines are checked for line width, whether the edges are well-defined, and the consistency throughout the line ($D6$). This is expected to give the answer to the second sub-question and as a result an answer to the main research question ($M3$).

2

Set-up development

This chapter explains the steps that are part of the set-up development. A more in depth explanation is given for the deposition configuration and variables within the set-up.

2.1. Experimental set-up

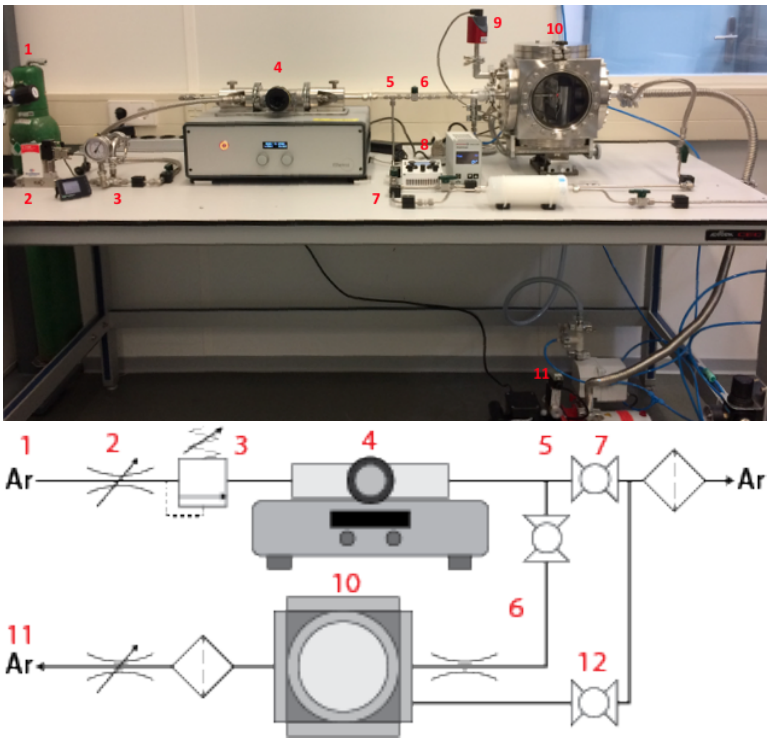

Figure 2.1: A photo and a schematic representation of the experimental setup. (1) argon flask (2) Bronkhorst High Tech El-Flow Prestige flow controller (3) overpressure valve (4) VSP G1 (5) Flow split (6) Deposition tubing (7) Waste tubing (8) XY-stage controller (9) CMR 362 Pfeiffer Vacuum gauge (10) Vacuum chamber (11) DUO-11M Pfeiffer Vacuum pump (12) Vacuum chamber vent line

The set-up used throughout this research is shown in Figure 2.1. In the set-up a carrier gas enters the system from an argon flask (1), the flow rate is controlled by a Bronkhorst High Tech El-Flow Prestige flow controller (2). An overpressure valve (3) is added before nanoparticle generation to prevent the release of aerosols in the environment. The tubing for transport of the carrier gas between sub-systems consists of 6.35 mm aluminum tubing. The VSP-G1 spark ablation machine (4) is operated in through-flow configuration, which means the carrier gas passes through both the hollow copper electrodes. The aerosol that exits the machine is split (5) into a deposition flow (6) and a waste flow (7). The deposition occurs in a vacuum chamber (10) which is equipped with a SmarAct SCL1750 ome-2 XY-stage and a controller (8). The aerosol inlet is

a 10 mm aluminium tube which fits different nozzles by clamp fitting. The chamber is connected to a DUO-11M Pfeiffer Vacuum pump by 20 mm tubing (11). It is equipped with the xy-stage, while the z-direction is controlled manually. The pressure within the vacuum chamber is measured by a CMR 362 Pfeiffer Vacuum gauge (9).

With this system, several situations can occur depending on the configuration and the process variables. Two situations are to be prevented, which is mainly dependent on whether the waste flow channel is blocked off or not:

- Q_{dep} is smaller than the choked flow rate between p_0 and p_2, as a result the Q_{dep} is increased by the flow reversing at Q_{waste}. If the flow rate, Q_{waste}, is equal to zero an under pressure is generated in the system.

- For Q_{waste} equal to zero and Q_{dep} greater than the choked flow rate between p_0 and p_2, the system builds up pressure.

Figure 2.2 shows a schematic of the deposition system. Section A allows for several nozzles. While section B allows for the placement of a restriction that limits the flow rate to Q_B. The deposition flow rate (Q_{dep}) is equal to the flow rate through the smallest restriction in A or B. With choked flows at both A and B, the pressure in between A and B (p_1)

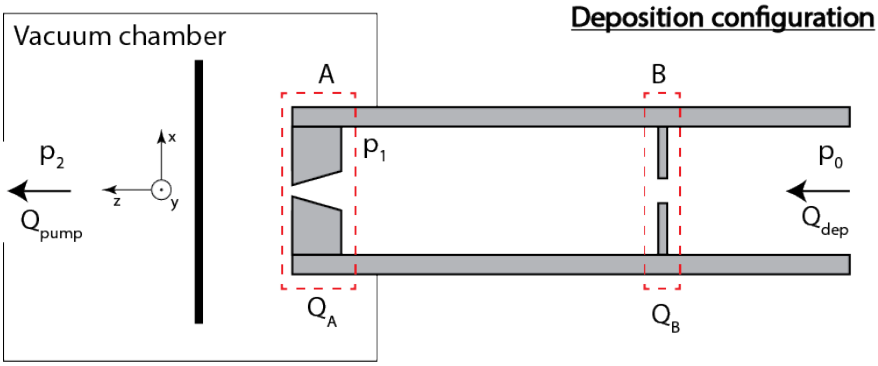

Figure 2.2: Schematic of the deposition system and the nozzle and restriction sections, A and B respectively, that determine the deposition configuration.

For general operation p_0 is at atmospheric pressure and p_2 is at medium vacuum. p_1 is dependent on the restriction at A and B, and for choked flows is calculated by Boyle's law, which assumes that pressure times volume stays constant. The restrictions are used to change the deposition methods or deposition variables. The situation is dependent on p^* as calculated by Equation 1.1. p^*/p_1 for argon at room temperature is equal to 0.49. The configurations considered in this work are:

- A restriction and a sonic nozzle. $Q_{dep} = Q_B$ with the ratio of p^*/p_1 smaller than the ratio in Equation 1.1; a sonic jet is formed at A, the flow after restriction B is also sonic.

- A restriction and a subsonic nozzle. $Q_{dep} = Q_B$ with the ratio of p^*/p_1 larger than the ratio in Equation 1.1; a subsonic jet is formed at A, the flow after restriction B is sonic.

- No restriction and a sonic nozzle. $Q_{dep} = Q_A$; a sonic jet is formed at A as $p_0 = p_1$.

2.2. Initial development steps

The development of the set-up took three major steps before it was able to perform the experiments discussed in Chapter 3. Since the knowledge attained in these steps were of major importance for the direction of the research, a short description is given for each step.

2.2.1. The analysis of microparticles

The initial system, built to reflect the manufacturers deposition system, used two configurations: the first with a restriction without a nozzle, while the second is a configuration with a restriction and a 1.5 mm diameter nozzle (subsonic deposition). Both configurations resulted in no deposits. The set-up was tested with a diverging sonic nozzle with a diameter of 0.7 mm which resulted in observable deposits. One of these deposits is illustrated in Figure 2.3. The SEM images shows similar areas as the scattered microparticle regions observed in later experiments. The deposits were not as expected due to the decreasing particle density while the particle size is similar throughout.

A rough comparison between the mass present on the substrate and the evaporated mass, shows that only a small part of the material is deposited. It was confirmed by the VSP-G1 manufacturer that 1 to 2 % of the generated mass are unwanted microparticles. More detail on the calculations of generated mass are given in Appendix B. The problem was analysed to be either due to the synthesis process not generating any nanoparticles, or due to the vacuum pressure being too high (approximately 50 $mbar$), and thus only the deposition of large particles occurs.

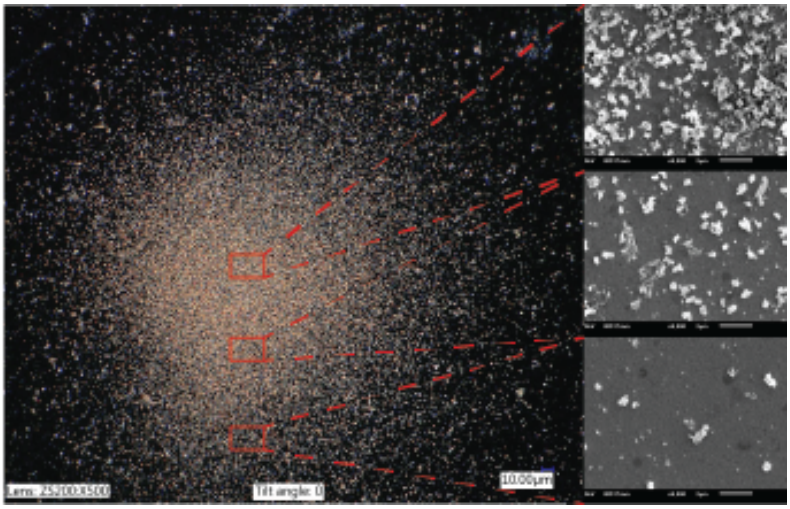

Figure 2.3: Optical image with three SEM pictures taken at different radial positions of the deposit.

2.2.2. Sonic nanoparticle deposition

In the second development step, the vacuum pressure was decreased to 24 $mbar$ by an improved sonic nozzle with a lower choked flow rate. The deposits contained nanoparticles on the edge of the deposit. The shape of the deposit is addressed in Section 4.3. The deposit and the uniform layer of nanoparticle agglomerates are given in Figure 2.4. It was noted that the uniform layer is only visible on the edges of the deposit while the centre is, again, characterised by the microparticle region, further denoted as micro-aggregate region.

The subsonic configuration initially showed no deposit. Since it could be concluded that nanoparticles are generated in the system, the vacuum pressure required a further decrease. However, before making further changes to the system, the effect of pressure on the sonic configuration was verified with the set-up available at the VSP. The experiment is described in Section 4.1.

2.2.3. Subsonic nanoparticle deposition

To decrease the vacuum pressure, an analysis was performed with a Pfeiffer Vacuum SmartTest vacuum and sniffing leak detector. The results showed that the flow through the tubing was choked at a lower value than the pumping capacity, which means a restriction limits the flow rate before the vacuum chamber. Additionally, the system was tested for leaks and it showed that the most significant leak was caused due to the ring seal which allows for movement in Z-direction. The removal of the restrictions between the vacuum chamber and pump, and an increase in tube size from 6.35 mm to 20 mm, resulted in pressures of approximately 2.4 $mbar$ without a deposition flow.

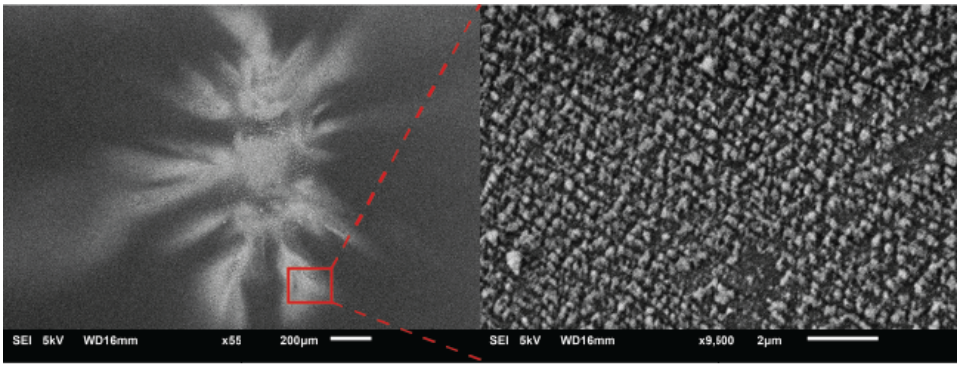

Figure 2.4: A sonic deposit (left) where nanoparticle agglomerates were observed in a uniform layer (right).

For deposition purposes, the smallest restriction available allows for a deposition flow rate (Q_{dep}) of 0.1 l/min. With this restriction, the minimum vacuum pressure with a deposition flow was found to be 3 $mbar$. In addition to improvements to the sonic configuration, the subsonic configuration also resulted in deposits like those found in Chapter 3.

2.3. System variables

The full system has a large amount of variables that can potentially influence the final deposit. This section gives more insight on the deposition configurations used throughout this work. In addition, an overview is given of the process variables that are of importance for the final deposit. Further information on how to operate the set-up is given in Appendix C.

2.3.1. Deposition configurations

The nozzles used in this research are manufactured on a lathe. As described in Chapter 4.3, a conical nozzle is used for the sonic experiments, since a conical nozzle shows less susceptibility to imperfections induced by the fabrication process. A thick plate nozzle is used for the subsonic experiments.

In addition, three restrictions with different flow rates are available (0.1 l/min, 0.7 l/min, 1.1 l/min). However, to reduce the vacuum pressure, the restriction of 0.1 l/min is used for all experiments.

Nozzles 2.5a and 2.5b have throat diameters of 2 and 0.3 mm respectively. The ratio of throat length to diameter is kept constant in accordance with research done in [61]. The throat in nozzle 2.5b conical to simulate a thin plate orifice. The effective throat length is reduced to less than 0.1 mm.

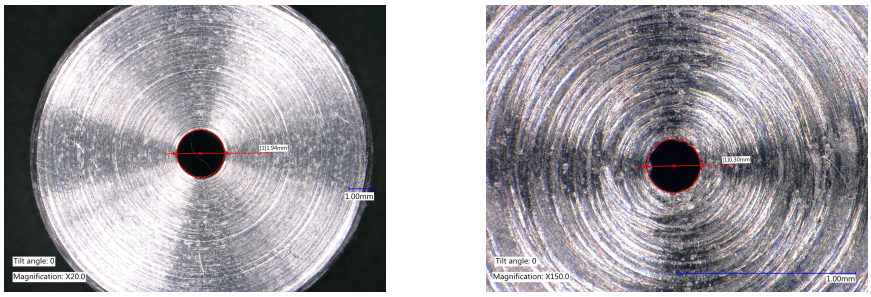

(a) Thick plate nozzle with a throat diameter of 2 mm and a depth of 2.5 mm.

(b) Conical nozzle with a throat of 0.3 mm, a depth of 0.1 mm, and a cone depth of 0.4 mm.

Figure 2.5: The two main nozzles used throughout this research.

2.3.2. Process variables

Table 2.1 gives an overview of variable parameters. The second column gives a description and the influences of the parameter. The categories are: Direct spark variables, which are set on the VSP-G1; Indirect spark variables, which though not set on the VSP-G1 are subject to change; flow variables, which influence a flow rate in the system; and deposition variables, which are the variables that influence the deposition.

Table 2.1: A list of variables that can be altered within the experimental setup.

Variable	Symbol	Description
Direct spark variables		
Spark voltage	U_s	The voltage set on the VSP G1.
Spark current	I_s	The current set on the VSP G1.
Indirect spark variables		
Breakdown voltage	U_{br}	The spark breakdown voltage (not equal to the spark voltage, as shown in Chapter B).
Spark frequency	f_s	The frequency of the spark between the electrodes, further elaborated in Chapter B.
Mass evaporated	m_{ev}	The evaporated mass from the electrodes, as calculated by [41]. More evaporated mass results in larger primary nanoparticles.
Flow variables		
Initial flow rate	Q_{in}	The flow set on the flow controller, a higher flow causes smaller primary nanoparticles due to the vapour being more diluted.
Deposition flow rate	Q_{dep}	The aerosol flow that is used in the deposition, controlled by the smallest restriction in the deposition tubing.
Waste flow rate	Q_w	The excess aerosol flow that is not used for deposition, determined by the difference between Q_{in} and Q_{dep}.
Pump flow rate	Q_{pump}	The effective pump flow rate at the vacuum chamber, controlled by a choking valve.
Deposition variables		
Substrate distance	L	The distance from nozzle to the substrate in the deposition chamber.
Spark pressure	p_0	The pressure in the VSP G1, generally equal to atmospheric pressure.
Restriction pressure	p_1	The pressure between the two restrictions, dependent on Q_{dep} and flow through restrictions.
Vacuum pressure	p_2	The pressure in the vacuum chamber, controlled by Q_{dep} and Q_{pump}.

3

Paper

This chapter contains the paper that discusses the results of this research. Additional information about the research is found in Chapter 4. A larger representation of the SEM image table and the experimental set-up is given in Appendix D.

Effect of Flow Conditions on Nanoparticle Aerosol Deposition for Direct Writing Purposes

B.G. Entink, S. Aghajani, L. Sasso, M. Tichem

Mekelweg 2, 2628 CD Delft

Abstract

Nanoparticles have unique properties that are sought after for the development and improvement of applications. The production of these applications require well-controlled environments. This work explores sonic and subsonic aerosol deposition for the direct writing of patterns of nanoparticle agglomerates. Three depositions configurations are analysed based on single spot deposition comparing the configurations based on the deposit shape, deposit pattern and surface morphology. In this analysis the deposition pressure ratio and the substrate distance were varied to find suitable process variables in addition to the most suitable configuration for direct writing. The applicability of the result for the direct writing of lines is experimentally confirmed by varying the variables of the nanoparticle generator. It is found that a sonic configuration with low pressure ratios has the smallest deposit diameter. Two main regions are visible in the deposits of this configuration, a micro-aggregate region and a nanoparticle region. The direct writing of lines shows that these different regions are influenced by the process variables of the nanoparticle generator, though all lines have a similar width. The viability of patterning with nanoparticle agglomerates, with a wide variety of particle sizes due to the limitations of the set-up, is proven by the direct writing of narrow lines with a width smaller than 400 μm. Since the set-up does not require a well-controlled environment, future research could lead to a direct writing system usable in manufacturing lines.

Keywords: Nanoparticles, Nanoparticle patterns, Spark ablation, Direct writing, Aerosol deposition

1. Introduction

The functionalities added by the unique properties of nanoparticles are widely researched, with success, for the development and improvement of applications. For example, nanoparticle thin films that add a transparent superhydrophobic layer [1] or improve the absorption of solar panels [2]. But also applications that require localised thin films or patterns are found in literature, like gas sensors [3] or conductive lines [4]. Though these applications are similar due to the use of nanoparticles, the fabrication processes differ substantially. For example, [1] immerses the samples in several aqueous solutions, while [2] deposits silver nanoparticles by thermal evaporation.

These works show that though the applications are plenty, further research is needed on a system that is able to manufacture a variety of applications and only requires limited additional processes. Consequently, a need exists for a high level of control over the deposition process of nanoparticles. Though ideally this control means the individual placement of each nanoparticle, the control considered here is that of deposit thickness, deposit particle density and the deposit diameter.

A promising method for patterning of nanoparticles are direct writing technologies (DW). The technologies aim to precisely deposit material, functional or structural, onto a substrate [5]. DW contains a large amount of different technologies like: inkjet printing [6], two-photon-polymerisation [5], liquid extrusion [5], and aerosol deposition [7]. For the patterning of nanoparticles, inkjet printing requires the nanoparticle to be in a liquid suspension [6], while two-photon-polymerisation and liquid extrusion do not aim to deposit nanoparticles [5]. However, aerosol deposition (AD), as the name implies, deposits nanoparticles mixed in a gas. Contrary to inkjet printing, no additional process that could influence the deposit is required to remove the medium in which the nanoparticles reside. This lack of additional processes is advantageous for the direct writing of different materials, however, it also brings additional challenges.

The motivation of this study is to explore the direct writing of aerosols with different deposition configurations and find the most suitable process variables for the direct writing of patterns. In this research, an investigation is started on the deposition of copper nanoparticle agglomerates suspended in argon. The nanoparticle agglomerates have a wide size distribution due to the nanoparticle synthesis process. The present work compares several deposition configurations for their applicability in direct writing.

The paper starts with a more in depth state of the art section, after which a theoretical background flow and particles in a flow is given to introduce the most commonly encountered variables in AD. The work continuous with a detailed explanation of the set-up used throughout the experimental work. The results are discussed in two sections, firstly the deposits are examined and compared based on the deposit shape, deposit diameter, the location of different nanoparticle agglomerate sizes, and the particle density. Secondly, the most suitable configuration and process variables are used for the writing of lines, followed by a discussion on the influence of different settings on the nanoparticle generator. This discussion is complemented by a more thorough analysis of the particles observed in the lines.

2. State of the art

Several approaches exist to deposit particles from an aerosol. Cold spray technology (CS) is mostly seen for applying coatings. The technology utilises high upstream pressure to reach sonic velocity jets that accelerate the particles and make them collide with the substrate and consequently attach to the substrate due to deformations [8]. Since CS deposits at atmospheric pressures, the drag is high and as a result the minimum particle size for deposition is higher than the particles considered in this work.

The deposition of smaller particles is done by aerosol deposition (AD)[9]. Though AD also includes the deposition of airborne liquid droplets, only aerosols with nanoparticles are considered in this work. AD utilises a low pressure deposition environment to reduce the drag on particles. This reduction of drag reduces the ability of particles to follow the flow lines accurately due to their inertia, and thus sharp flow bends induced by a substrate cause particles to impact the substrate [10]. The particle deposition occurs by particle deformation on impact, as seen for CS, and still requires further research to be fully understood [9]. A possible deposition window compared to that of CS is given in [8], and shows deposition at lower velocities.

Work on impactors, though it does not involve characterisation of the deposits, aims to filter the smallest of particles by similar means as CS. However, as seen for CS, the deposition of nanoparticles requires additional measures. Though several types of impactors exist, the main interest for this work is the low-pressure impactor since it shows the best resemblance to AD. Additionally, the research on impactors aims to collect all the particles larger than a specific size [11]. This type of research is specifically of interest for the system to have higher deposition efficiencies. Hence, the work on impactors contains vital information on the conditions at which particles deposit.

The focusing of particles of subsonic jets often occurs by aerodynamic lens systems, that focus nanoparticles to the jet centre line by consecutive convergences, or so-called lenses [12, 13, 14]. In [13] such a system was optimised and was able to focus 5-50 nm particles at relatively high downstream pressure (4.25 $mbar$). The simulations of this study show that the smaller particles deposit over a larger area, which is in agreement with the expectations that these particles follow the flow more accurately. This effect is increased further when diffusive effects are added to the simulations. However, the diffusive effect also causes the larger particles of 100 nm to deviate further from the jet centre line than the 30 nm particles [13]. The work shows that a lens system designed for a certain size, causes significantly larger particles to end up further from the deposit centre.

Similarly, [10] reviewed the focusing of particles for different types of nozzles. Specifically of interest is the difference between deposition by a capillary or thin plate orifice. While for the capillary nozzle the particles focus on the centreline within the nozzle, with a radial particle size distribution [15], the conical nozzle, focuses the particles after the nozzle [16]. The focusing effect for the conical nozzle is dependent on particle size, with the focus point further away for small particles. This effect is also seen in [13], where the last lens in the system is a conical nozzle.

3. Theoretical background

For the categorisation of flow type, two types are considered: subsonic and sonic. Whether a flow is sonic or subsonic is dependent on the ratio between the downstream pressure (p_2), and upstream pressure, (p_1). The flow is subsonic when the value of p_2 is higher than a critical value, p^*, while lower values of p_2 result in a sonic flow. The critical value is calculated by Equation 1 [17], where γ is the heat capacity ratio of the gas. Thus, categorised by the flow type, this theory indicates the availability of two types of AD, controlled by the upstream and downstream pressures.

$$\frac{p^*}{p_1} = \frac{2}{\gamma + 1}^{\frac{\gamma}{\gamma - 1}} \tag{1}$$

A free subsonic jet shows a constant divergence of the jet paired with a deceleration of the flow. A sonic free jet is contained by a jet boundary and accelerates due to rapid expansion of the gas. For the sonic jet a Mach disk occurs, at a distance L_m, as calculated by Equation 2 where d_n is the nozzle diameter. After the Mach disk, a similar flow development occurs as from the nozzle, though with less energy. When the energy level descends below a critical point, the sonic flow continues as subsonic flow.

$$L_m = 0.67\, d_n \sqrt{\frac{p_1}{p_2}} \tag{2}$$

Figure 1 shows schematics of impinged jets of both the flow types. The impinged subsonic jet diverges and the flow is bent around the substrate, creating a stagnation

point where the flow velocity is zero. The sonic impinged jet accelerates after the nozzle, and is contained by the jet boundary. Close to the substrate, a so-called bow-shock is caused, where the flow compresses to the subsonic regime. In this subsonic regime, a stagnation point and region is found similar to that of a subsonic impinged jet. Literature [18] shows that the collection efficiency of nanoparticles is higher for bow-shocks that are closer to the substrate. The variation of bow-shock distance (δ) from the substrate for different nozzle diameters and pressure ratios versus the nozzle to substrate distance is given in [18]. The flow parallel to the substrate are wall jets, for which the velocity is dependent on pressure ratio between the compressed flow and vacuum chamber and can reach sonic velocities.

Since after the first Mach disk a similar flow development occurs, it is expected that most deposit changes are found between the nozzle and the first Mach disk. Additionally, the bow-shock distance from the substrate is dependent on the placement relative to the distance L_m, thus influencing the deposition [18]. Hence, L_m is expected to be of importance for the sonic deposition. Since L_m is dependent on the pressure ratio, the effect on the deposit is analysed by changing p_1/p_2.

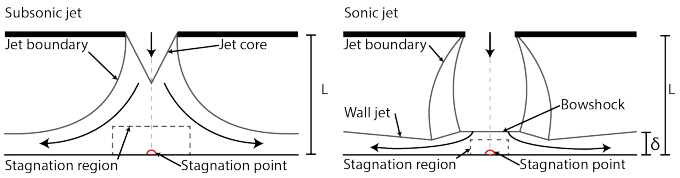

Figure 1: Schematic of an impinged subsonic jet (left) and an impinged sonic jet (left).

The particle behaviour within jets is characterised by the dimensionless Stokes number. The number gives an indication of the ability of the particle to escape the flow lines, which in the case of aerosol deposition is necessary for the particle to collide with the substrate. The Stokes number is given in Equation 3 and relates the particle stopping time (τ_p) to the characteristic time of the flow (τ_f). Values much greater than unity cause particles to escape the flow while for much smaller values particles follow the flow accurately. Intermediate values result in only slight deviations from the flow lines [10], consequently influencing the radial position of deposition. The Stokes number is often determined experimentally, however a correlation is given in Equation 3 [14], with the average jet velocity at the nozzle, u_0, and d_n equating to τ_f. ρ_p and μ_0 are the material dependent particle density and gas viscosity respectively. It should be noted that the Equation calculates the Stokes number at the nozzle. The correlation shows the quadratic dependence on particle diameter (d_p) which results in the smallest particles meeting the requirements for impact the furthest away from the jet-centre line. C_c is the Cunningham slip correction and accounts for the lower drag force on sub-micron particles due to slip. The correlation is given by Equation 4 [14] where λ is the free mean path of the gas. λ increases with a higher vacuum and consequently the Stokes number. As given in [13] it is expected that besides the Stokes value, the higher diffusive effects on small particles influence the deposit area, and thus the smaller agglomerates of nanoparticles deposit over a wider area than the larger agglomerates.

$$Stk = \frac{\tau_p}{\tau_f} = \frac{\rho_p \, d_p^2 \, C_c \, u_0}{18 \, \mu_0 \, d_n} \tag{3}$$

$$C_c = 1 + \frac{2\lambda}{d_p}(1.257 + 0.4e^{\frac{-1.1 d_p}{2\lambda}}) \tag{4}$$

The impact of nanoparticles on a substrate, requires the particles to have Stokes numbers above a critical value. The research that works on further development of impactors often gives this value close to unity [19, 20]. However, the particles with bigger Stokes numbers deposit closer to the jet centre-line. From the two equations, two methods of increasing the Stokes number are relevant for this study. The first is an increase in average jet velocity. The sonic flow development however, reaches an asymptotic limit for the jet velocity at v_{max}, as given in Equation 5, where k is the Boltzmann constant, T_0 is the stagnation temperature of the gas and m is the molecular mass of the gas [21]. Both [18] and [21] claim that v_{max} is reached at approximately ten times the nozzle diameter for sonic flows with high p_1/p_2. Additionally, subsonic deposition is limited by the speed of sound of the gas. However, literature also shows that the particle impact velocity influences whether impact causes attachment or a different phenomena, like bounce and de-agglomerated particles [22]. The second method is to gain a lower vacuum pressure and consequently increase the Cunningham slip correction.

$$v_{max} = \sqrt{\frac{2\,\gamma}{\gamma - 1}\frac{k\,T_0}{m}} \tag{5}$$

Table 1 shows the parameters that are linked to the downstream pressure (p_2) and the substrate distance (L) for subsonic and sonic flow. For subsonic flows, p_2 influences the average jet velocity at the throat (u_0) and the particle drag, which the Cunningham slip correction (C_c) accounts for. Both u_0 and C_c increase for lower downstream pressures, consequently increasing the Stokes number. Since the Stokes number has a quadratic dependence on the particle diameter (d_p), this increase causes smaller particles to reach intermediate Stokes values. L however, decreases the jet velocity after the throat due to the divergence of a subsonic jet for larger value of L.

The influence of both p_2 and L are different for sonic flows. p_2 influences the particle drag similar to that of subsonic flows, however, the velocity at the throat is limited by the speed of sound. The ratio p_1/p_2 influences the flow development and higher values are expected to increase the jet diameter. The influence of L differs significantly,

since the sonic jet accelerates after the nozzle. The distance over which the jet accelerates is dependent on L_m, which is dependent on p_1/p_2 [18].

In conclusion, for subsonic deposition a lower pressure increases the Stokes number, and is thus advantageous for the deposition of smaller particles. However, an increase in substrate distance decreases the Stokes number. For sonic deposition a lower pressure is also advantageous, however high pressure ratios are expected to increase the jet diameter. The substrate distance is expected to increase the Stokes number, with the largest increase found between the nozzle and the Mach disk.

Table 1: Process variables for the three configurations.

		Subsonic
p_2	p_1/p_2	The jet is a result of the ratio between upstream pressure (p_1) and downstream pressure (p_2) ratio with $p_2 > p^*$, where p^* is the critical downstream pressure, and influences the jet velocity.
	λ	The gas mean free path influences the particle drag, and is implemented in the Stokes number through the Cunningham slip correction (C_c).
L	u_0	The jet diverges and decelerates for larger distances.
		Sonic
p_2	p_1/p_2	The jet is a result of the pressure ratio with $p_2 < p^*$, and influences the jet velocity.
	L_m	The Mach disk distance (L_m), is dependent on the square root of the pressure ratio and influences the flow development.
	λ	The gas mean free path (λ) influences the particle drag, and is implemented in the Stokes number through C_c.
L	u	The jet accelerates after the nozzle and decelerates before L_m.

4. Experimental Methods

This work explores how pressure and substrate distance influence the deposition of an aerosol that contains agglomerates of nanoparticles with a wide size distribution. Specifically, an analysis is done on the deposit shape and deposit patterns. The set-up is based on a nanoparticle generator that generates an aerosol which can then be directly deposited on a substrate in a vacuum chamber.

The experimental set-up is schematically illustrated in Figure 2. In the set-up a carrier gas enters the system from an argon flask (1), the flow rate is controlled by a Bronkhorst High Tech El-Flow Prestige (2) that allows for an inlet flow (Q_{in}) between 0.15 l/min to 20 l/min. An overpressure valve (3) is added before nanoparticle generation to prevent the release of aerosols in the environment. Aluminium tubing with an inside diameter of 6.35 mm is used to transport the carrier gas. The VSP G1 (4), synthesises nanoparticles by a spark ablation process. The aerosol that exits the machine is split in a deposition flow (5) and a waste flow (6). The deposition occurs in a vacuum chamber (7) which is equipped with a SmarAct SCL1750 ome-2 XY-stage (8), while the z-direction is controlled manually. The pressure in the chamber is measured by a CMR 362 Pfeiffer Vacuum gauge. The aerosol inlet is a 10 mm aluminium tube which fits different nozzles by clamp fitting. The chamber is connected to a DUO-11M Pfeiffer Vacuum pump (9) by 20 mm tubing. Opening the ball valve (10) vents the vacuum chamber.

In the VSP G1 the spark is controlled by a voltage set point (U_s) with a range of 0.01 kV to 1.36 kV and a current set point (I_s) with a range of 0.1 mA to 10.4 mA. The current set point also sets the spark frequency (f_s). The argon flows through the electrodes and transports the vapour cloud (11). The amount of material that is ablated with each spark is dependent on I_s as given by [23]. The vapour cloud coalesces due to rapid quenching by the argon. The phase results in primary nanoparticles (12). The size and amount of primary nanoparticle is dependent on the amount of material per volume [24], thus I_s and Q_{in}. Starting at the end of the coalescence phase until the deposition the primary nanoparticles agglomerate due to collisions (13). The aerosol also contains micro-sized particles that are expected to be chunks of electrode material which did not vaporise completely.

The aerosol flows through the deposition system which consists of two variable sections, a nozzle (A) and a restriction (B), which are 300 mm apart. B has either no restriction ($p_0 = p_1$) or a critical orifice for which Q_b is 0.1 l/min. The restriction changes the pressure from p_0 to p_1 due to a choked flow. Two different nozzles are used at A, a flat-plate nozzle, which has a round throat with a diameter and depth of 2 mm, and a conical nozzle, similar to the schematically drawn nozzle in Figure 2, that has a throat diameter of 0.3 mm, a throat depth of 0.1 mm and a conical depth of 0.4 mm. The flat plate nozzle requires a restriction to reach the minimum flow required for deposition. The choked flow rate of the conical nozzle is 1.2 l/min. The result is three possible configurations:

1. The flat plate nozzle with restriction, which results in a subsonic jet.
2. The conical nozzle with restriction, which results in a sonic jet where p_1 is calculated by Boyle's law to be 12 times lower than atmosphere due to the ratio between Q_a and Q_b.

3. The conical nozzle without restriction, which results in a sonic jet where p_1 is equal to atmospheric pressure ($p_1 = p_2$).

A Keyence Digital Microscope VHX-6000, a Jeol JSM-6010LA (SEM) and a FEI NovaNano SEM (HR-SEM) are used for optical and electron microscopy. The effect of pressure, pressure ratio, and substrate distance (p_2, p_1/p_2 and L) on the deposit shape, deposit diameter, location of nanoparticle agglomerates and particle density is analysed for single spot deposits for each configuration. The effect of spark ablation variables (Q_{in}, U_s and I_s) on the particle density, particle size, and particle distribution is analysed with the patterning of lines. The lines are patterned with the configuration and variables that are deemed most suitable. The copper nanoparticles are collected on glass for the single deposit and on boron doped silicon wafer for the lines.

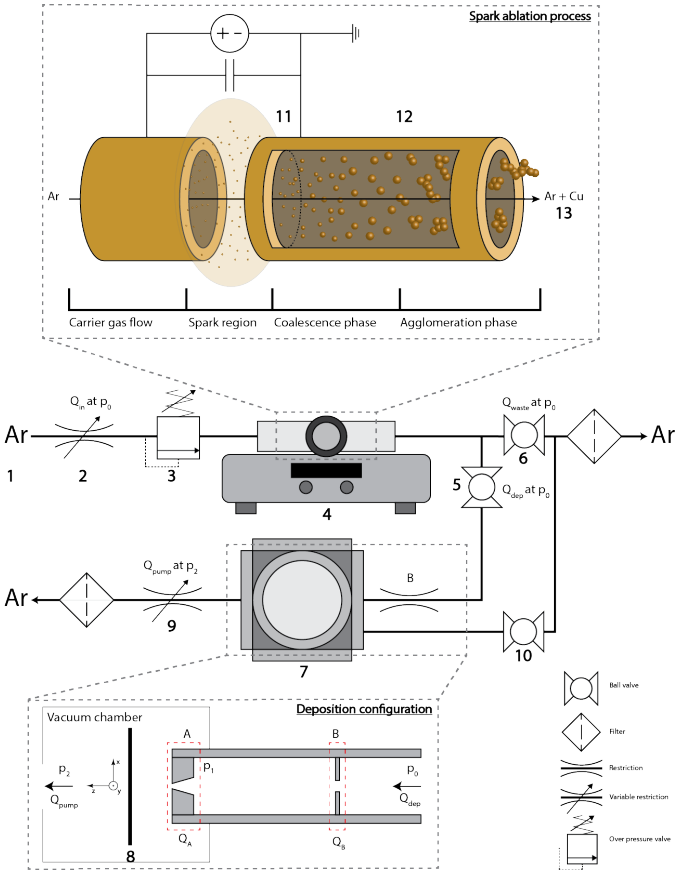

Figure 2: Schematic overview of the experimental set-up with the following components: (1) Argon inlet (2) Bronckhorst High Tech El-Flow Prestige flow controller (3) Overpressure valve (4) VSP G1 (5) Deposition flow (6) Waste flow (7) Vacuum chamber (8) SmartAct SCL1750 ome-2 XY-stage (9) DUO-11M Pfeiffer Vacuum pump (10) Vacuum vent channel. The spark ablation inside the VSP G1 allows for argon to flow through the electrodes, transporting away the material in the spark region. The material coalesces up till a critical size, the primary nanoparticles. The primary nanoparticles agglomerate up till the deposition. The deposition configuration consists of two sections, the nozzle (A) and a restriction (B).

5. Experimental analysis of aerosol deposition configurations

As mentioned, the differences between the three configurations are examined by a variation in vacuum pressure (p_2), which influences the jet velocity and Cunningham slip correction, and the nozzle to substrate distance (L) to see the influence of the jet development on the deposition process. The variables for each configuration are given in Table 2. L is varied in 8 steps with intervals of $1/3$ mm starting at $1/3$ mm.

The single spot deposits, as given in Figure 3, show different deposit regions. The dark spot (a) is the centre of the deposit which mainly contains micro-sized particles, hereinafter referred to as micro-aggregates. The region around the dark spot (b) shows scattered micro-aggregates and a layer of the larger agglomerates of nanoparticles. The micro-aggregates closest to the jet centre line have the highest Stokes numbers due to their particle diameter, and consequently deviate less than the nanoparticle agglomerates. It is expected that the scattered micro-aggregates are due to a particle distribution in the flow through the nozzle. The area around the micro-aggregates (c), when observed with a collimated white light beam, shows several repetitions of the visible light spectrum. These so-called Fizeau fringes are due to optical interference between the reflections of the glass substrate and the layer of copper particles [25]. The order of the colour spectrum indicates that the thickness of the layer decreases radially. The layers are a uniform layer of nanoparticle agglomerates of which the particle size decreases radially. In Section 6.2 a more in depth analysis is given on the micro-aggregates.

Figure 4 shows SEM images of the deposits and are discussed separately for each configuration. The table shows the variation of L over the y-axis (for convenience divided by the diameter of the conical nozzle) and the different configurations over the x-axis.

Table 2: Process variables for the three configurations.

p_2	p_1	U_s	I_s	Q_{in}	Q_{dep}
$mbar$	$mbar$	kV	mA	l/min	l/min
Configuration 1					
3.5	-	1.2	6.0	0.5	0.1
10.0	-	1.2	6.0	0.5	0.1
Configuration 2					
3.5	85	1.2	6.0	0.5	0.1
10.0	85	1.2	6.0	0.5	0.1
Configuration 3					
10.0	1013	1.2	6.0	1.5	1.2
20.0	1013	1.2	6.0	1.5	1.2

5.1. Configuration 1: flat-plate nozzle with restriction

Configuration 1 deposits with a subsonic jet and utilises the flat-plate nozzle in combination with the restriction.

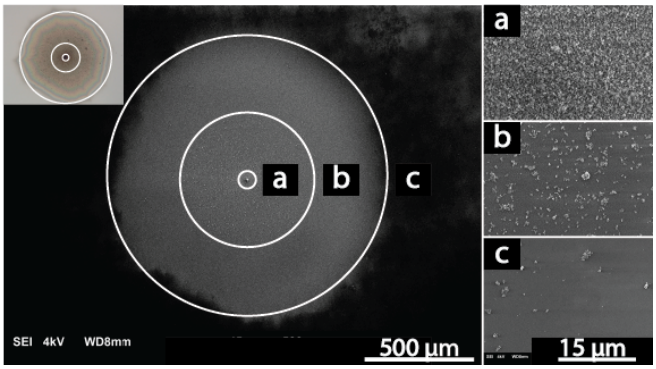

Figure 3: Images that indicate several regions in a deposit. The three regions found in both the SEM image and the inset (optical microscopy) are indicated by the white circles and additional SEM image are given to show the difference for each area. a) Dark centre with a high density of micro-aggregates, the precise centre is observed as seen in Figure 6a. b) Scattered micro-aggregates on a layer of nanoparticle agglomerates. With optical microscopy observed to be copper coloured. c) Layer of nanoparticle agglomerates with only a small number of micro-aggregates. With optical microscopy observed as Fizeau fringes.

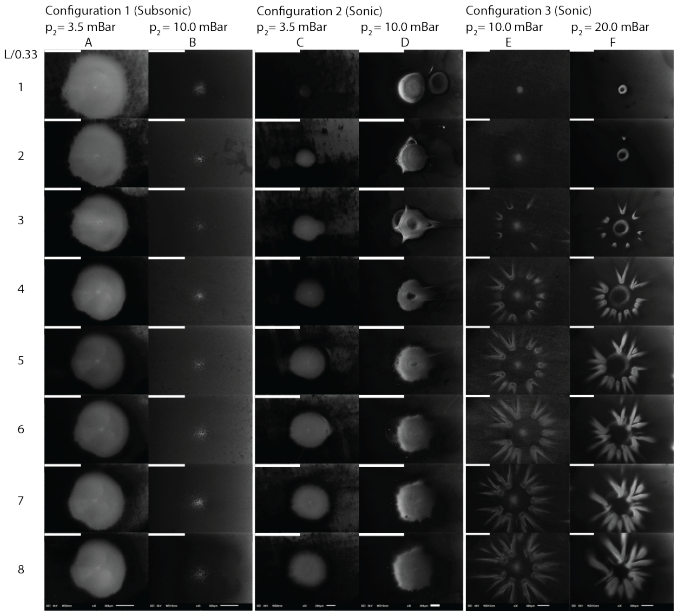

Figure 4: SEM images of the deposits of different configurations with varying pressure (p_2) and substrate distance ($L/0.33$). The top-left scale bars of each image are 1 mm. Each column is indicated by a letter, while the rows are indicated by numbers.

The images in column A and B in Figure 4 show that the deposits differ only slightly with L. In contrast, the variation in p_2 drastically changes the deposit shape. The graphs in Figure 5 illustrate the variation of deposit diameters with L for the two pressure levels. Though there are limits with observing nanoparticles by optical microscopy, the optical microscope gives the most consistent images and is thus used for the measurements. The measurement of the outer deposit diameter contains the whole visible deposit with the centre at the micro-aggregate region. The graph contains a horizontal line which indicates the nozzle diameter. Graph b lacks the outer deposit regions due to no observable nanoparticle region around the scattered micro-aggregates. The SEM images, Column B in Figure 4, show a similar result. This observation implies that either the deposition of nanoparticle agglomerates does not occur, or that the deposition only occurs in the micro-aggregate region. However, from the provided theory it is concluded that the smaller particles deposit in a larger area. Hence, nanoparticle agglomerates are not deposited as a result of a low jet velocity and high drag due to the increase of p_2, of which a more thorough investigation is given in Chapter 4.

The micro-aggregates experience a different focus effect than the agglomerates of nanoparticles. Graph a shows that the deposit diameters are below the nozzle diameter and only diverge slightly with L. Hence, the nozzle focuses the particles to a certain extent. In contrast, the micro-aggregate deposit diameter diverges with L and follows the expectations of an impinged subsonic jet. Both particle types are assumed to experience capillary focusing between the restriction and nozzle due to the tubing. In addition, the nozzle creates a focus effect. In [12] the focus effect of the agglomerates of nanoparticles is more favourable for an abruptly converging nozzle than that of capillaries. The work in [16] investigates the focus effect of capillary nozzles and shows that the optimum particle size increases for longer capillary nozzles with a depth to nozzle diameter ratio between 2 and 40. The nozzle utilised in the experiments of this work only has a ratio of 1 and is considered a thick plate orifice.

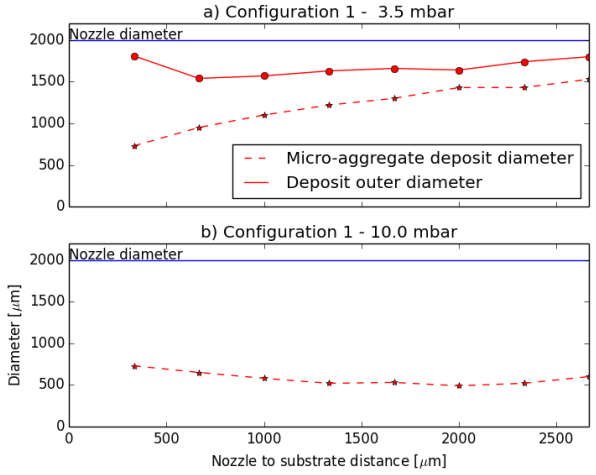

Figure 5: The graphs display the variation in diameter due to the nozzle to substrate length of both the micro-aggregates and nanoparticles.

Figure 6 shows four SEM images of different positions of a subsonic deposit, indicated by each inset. The centre of the deposit, a, is a stack of micro-aggregates. Image b

shows the micro-aggregates around this centre at higher magnification and shows a dense and rough surface. Radially outwards the particle density of micro-aggregates decreases and a less rough surface becomes visible which consists out of nanoparticle agglomerates, as seen in *c*. Image *d* is further radially outwards than *c* and shows a a further decrease of micro-aggregates. The nanoparticle agglomerates in *d* are smaller than those in *c*. The difference is due to the quadratic dependence of the Stokes number on the particle diameter, causing the smaller particles to deposit on the edges.

Ideally, the deposition flow shows axial symmetry. The deposit pattern (skull pattern), clearly visible in the insets in Figure 6, consists of three denser areas that show vertical symmetry for the insets. Additionally, the skull pattern shows the visible colour spectrum when the optical microscope is used with collimated white light. The SEM images in Figure 4 vaguely shows this same pattern in column *A*. By rotation of the restriction, and observing a similar rotation in the pattern, it is concluded that the pattern is related to the round restriction upstream of the nozzle. However, no similarities are found between the restriction shape and the deposit pattern. More details are given in Chapter 4.

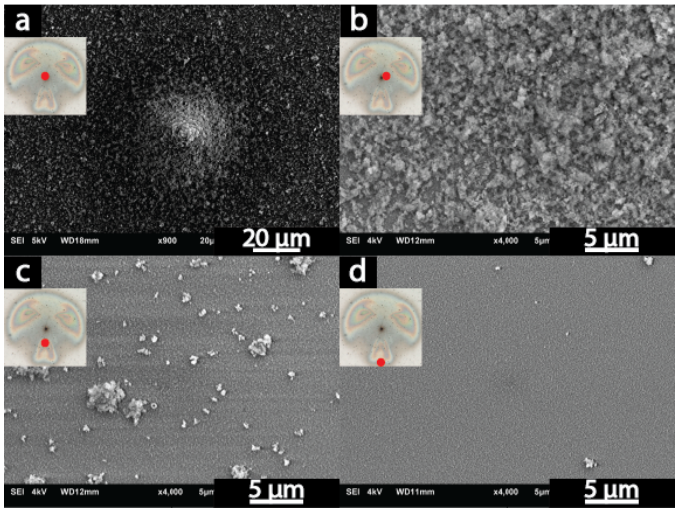

Figure 6: SEM images of the centre, slightly away from the centre, half the radius, and the edge of a deposit made by configuration 1 at high pressure at deposit distance 1 *mm*.

Since configuration 1 shows deposits of a smaller size than the nozzle diameter, as given in Figure 5, it is expected that a reduction of nozzle diameter results in smaller deposit diameters. However, to stay within the subsonic regime, and thus have a similar result, the pressure ratio has a limit as given by Equation 1 and thus consequently requires a further reduction of the restriction.

5.2. Configuration 2: Conical nozzle with restriction

Configuration 2 deposits with a sonic jet and utilises the conical nozzle in combination with the restriction. This combination results in a lower pressure at p_1, consequently reducing the pressure ratio p_1/p_2. Figure 4 column *C* and *D*, illustrate the increase in deposit size with L and a slight change in deposit shape with pressure ratio, as further illustrated by optical measurements in the two graphs in Figure 7. Since the variables in sonic flow theory are dependent on the nozzle diameter, d_n, the x-axis of the plots is changed from L to the ratio L/d_n. The vertical line in the plot indicates L_m, while the horizontal line indicates d_n.

The graphs show that for both pressure ratios the deposition diameter diverges with increase of L/d_n. Additionally, though the deposit diameter is smaller than that of configuration 1, the deposit diameter is always larger than d_n. Graph *a* shows a rapid divergence of the spot diameter; the diameter starts slightly larger than d_n and increase to three times d_n. Graph *b* diverges at a slower rate, and diverges from two times d_n to three times d_n. It is expected that a majority of the particles end up in the jet boundary of the sonic jet due to the rapid expansion. This also explains that L_m does not influence the deposits, since the jet boundary in a free sonic jet only diverges.

Graph *b* shows an additional line that indicates an empty inner centre which is visible with optical microscopy. This observation is attributed to a lower particle velocity and higher drag causing the largest agglomerates of nanoparticles and the micro-aggregates to have intermediate Stokes values and deviate from the jet centre line. In contrast, the higher pressure ratio has a clear centre point in the deposit for smaller substrate distances, as given in graph *a*. However, the SEM images in Figure 4 show this empty centre only at *D*3 and *D*4. For the other images the centre is visible but contain nanoparticles.

The images in Figure 8 are four SEM images of the deposits of Figure 4 Column *C*. The inset indicates the corresponding location within the deposit. Similar to configuration 1, the centre consists mainly of micro-aggregates. Additionally, the amount of micro-aggregates decrease radially outward, as seen in *b*. A comparison between *b* and *c* shows a difference in roughness of the nanoparticle layer. Image *d* illustrates this difference with a lower magnification. The image shows a uniform layer of nanoparticles for which the particle size decreases radially outward.

Figure 9 shows similar images for the lower pressure ratio (Column *D*). The centre of the deposit (*a*), though empty when observed with optical microscopy, shows scattered micro-aggregates with nanoparticle agglomerates in between. However, the layer of nanoparticle agglomerates is not a dense layer as that seen in for Figure 8d. The micro-aggregate region (*b*), earlier observed in the centre,

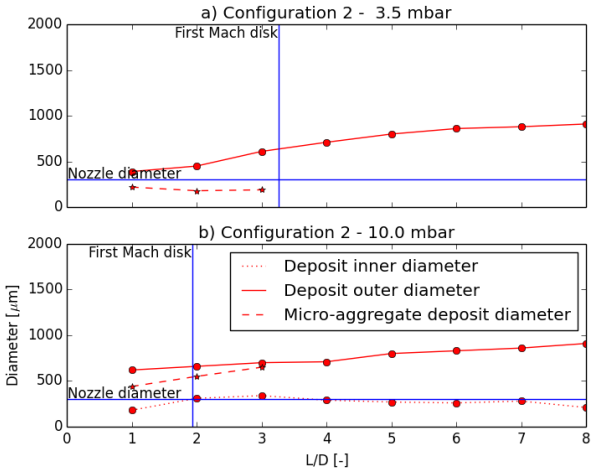

Figure 7: The graphs display the variation in diameter due to the nozzle to substrate length of both the micro-aggregates and nanoparticles.

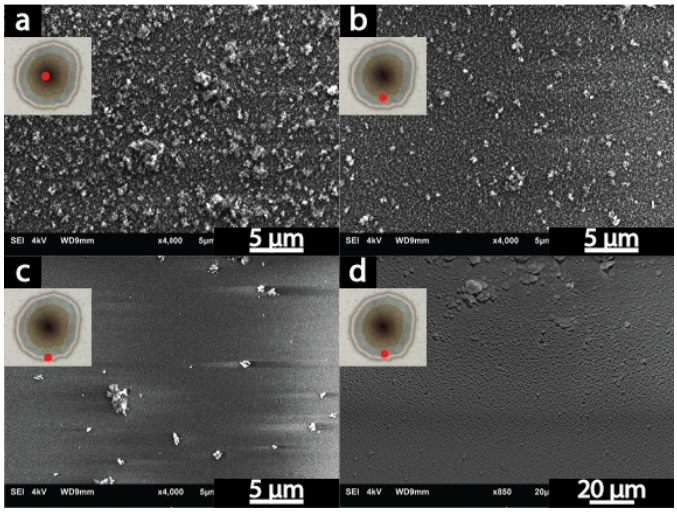

Figure 8: SEM images of the centre (a), half the radius (b), and the edge (c) made by configuration 2 at 3.5 *mbar* at deposit distance 1 *mm*. (d) shows the particle size gradient at the edge of the deposit.

is a ring around the centre. This observation indicates that though the micro-aggregates are larger, a lower pressure ratio causes them to deviate from the centre-line. The edge of the deposit differs in comparison to Figure 8c: the edge characterises itself by larger nanoparticle agglomerates in a less dense layer. Another thing observed only for this configuration are the stripes outward (d), the stripe has a sharp edge behind which particles are accumulating. Currently, no reason is found for the occurrence of these stripes.

In comparison, configuration 2 allows for a wider range of the pressure ratio than configuration 1 due to not being limited by the speed of sound. The deposit shape shows a circular deposit for both pressures and in comparison to configuration 1, no skull pattern is visible. This observation implies that the conical nozzle removes the focus effect caused by the restriction. Additionally, the deposits of configuration 2 have smaller deposit diameters than those of configuration 1, thus narrower lines are possible. The lower pressure ratio shows, as of yet unexplained, stripes radially outwards, as seen in Figure 4 for deposits $D2$, $D3$ and $D4$. Consequently, the lower pressure ratio is less suitable for direct writing. For configuration 2, a high pressure ratio with close substrate distances shows the most circular and smallest deposits. The circular shape causes the uniformity of patterned lines to be independent of writing direction, while the small deposit diameter results in the narrowest lines.

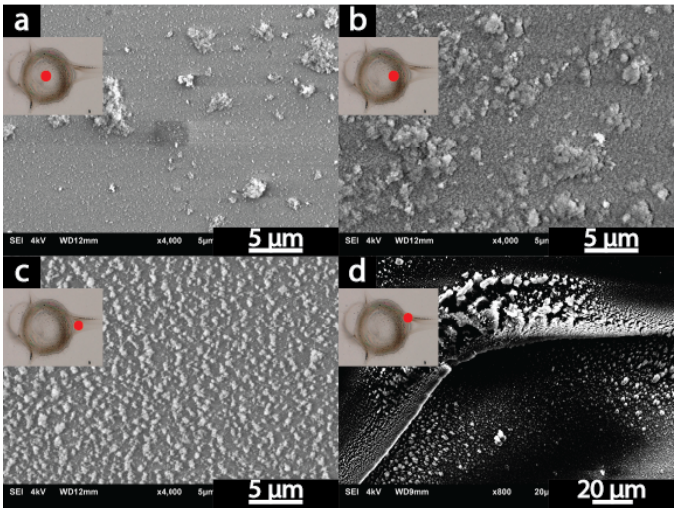

Figure 9: SEM images of the centre (a), half the radius (b), and the edge (c) made by configuration 2 at 10.0 *mbar* at deposit distance 1 *mm*. (d) one of the edges where a dark colour is observed in the optical images.

5.3. Configuration 3: conical nozzle without restriction

Configuration 3 deposits with a sonic jet and utilises the conical nozzle without restriction. As a result the configuration has the highest pressure ratios, and thus reaches the highest velocities. Figure 4 column E and F show that the deposit shape changes for both pressures with L/d_n. Since the nozzle has a larger choked flow (1.2 l/min) than the restriction (0.1 l/min), the pressure levels are at 10.0 *mbar* and 20.0 *mbar*. Additionally, Q_{in} is to 1.5 l/min. Figure 10 shows the deposit inner diameter, the deposit outer diameter and the diameter of the wall jet deposits.

Graph a shows a micro-aggregate region that stays at a comparable size as d_n for all substrate distances. However, at $L/d_n = 4$ deposition shape changes (see Figure 4) into a micro-aggregate region with outgoing stripes, measured as the diameter where the stripes start appearing. These stripes are further referred to as wall jet deposits. Contrary to graph a, the outer diameter of the micro-aggregate region diverges faster in graph b and increases above the wall jet deposition diameter. The wall jet deposits diameter converges with L/d_n, more clearly seen in graph b.

The centre of the deposits of column E are similar to those in column B and C, a clear centre and only slightly diverging with the substrate distance. The deposits in column F clearly show the inner diameter of the micro-aggregate region. This region is similar to that found for column D. However, contrary to column D the inner diameter is visible for all substrate distances. This observation is assumed to be due to the lack of nanoparticle agglomerates throughout the whole deposit, which were observed to be in the centre, as illustrated by Figure 9.

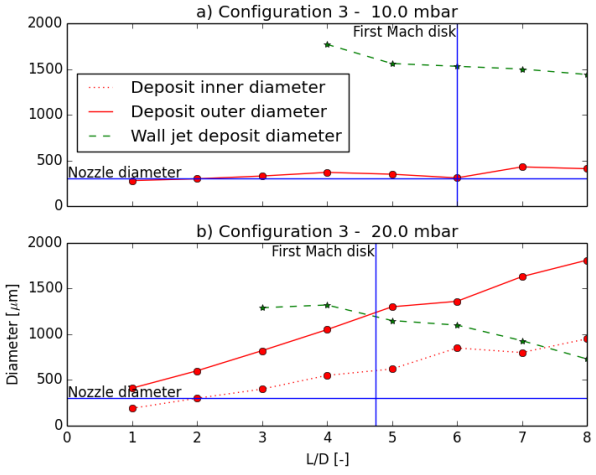

Figure 10: The graphs display the variation in diameter due to the nozzle to substrate length of both the micro-aggregates and nanoparticles.

The outwards stripes are assumed to be due to the turbulent wall jets that move parallel to the substrate. Figure 11 shows a SEM and optical image of the wall jet deposit. The width of the wall jet deposit increases with the radius and indicates an outward flow direction. The wall jet deposits have larger particles surrounded by a nanoparticle layer. The layer of nanoparticles behind the largest particles shows a less dense area with still relatively large particles. The larger particles have a uniform layer of nanoparticles around it, for which the particle diameter decreases away from the larger particles. The optical image (b) shows the Fizeau fringes and indicates a thinner layer on the edges of the wall jet deposit, supporting the observations in the SEM.

In comparison to configuration 1 and 2, configuration 3 has the smallest deposit diameters. However, the deposit shows similarities with the micro-aggregate region of configuration 1 with high p_2. The lack of observable nanoparticles in the centre or around the micro-aggregate region indicates a lack of deposition. Additionally, the appearance of wall jet deposits implies a large amount of the nanoparticles not impacting at the centre.

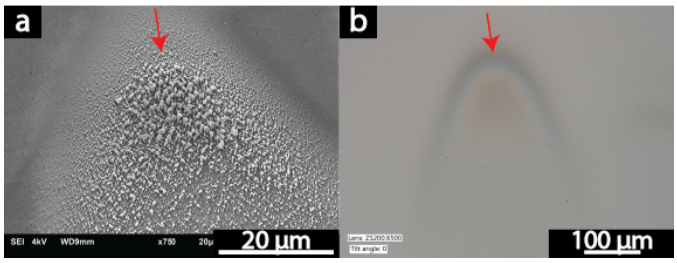

Figure 11: SEM image (left) and optical image (right) of the wall jet deposition of configuration 3. The red arrow indicates the flow direction, away from the centre.

5.4. Comparison

As expected the subsonic configuration, characterised by the lower average jet velocity, requires a higher vacuum to deposit nanoparticles than the sonic configurations. In the sonic configurations there is a clear difference in the two different pressures. The low pressure ratios are assumed to cause intermediate Stokes numbers even for the larger micro-aggregates. In support of this assumption is the less dense centre area, observed for the low pressure ratios of configuration *2* and *3*. The deposits of configuration 2 with a low pressure ratio additionally show a nanoparticle layer by Fizeau fringes. The presence of the nanoparticles in the jet of configuration 3 is however confirmed by the wall jet depositions that occur for larger nozzle to substrate distances.

When considering the experiments with vacuum pressures of 3.5 $mbar$, it is clear that the deposition of nanoparticles occurs for the full range of nozzle to substrate distances. Specifically for configuration 1 using subsonic velocities, this observation indicates that though the velocity is of importance, the reduced drag due to the Cunningham slip correction has a severe influence on whether deposition occurs.

Configuration 1 is not suitable for deposition of narrow lines. The deposit diameter is larger than the deposit diameters of configuration 2 and 3. To deposit with a subsonic jet limits the pressure ratio and thus requires a smaller restriction in addition to a smaller nozzle diameter. In contrast, configuration 2 has no limit to the pressure ratio, thus allows for a smaller deposit diameter without a change in restriction. However, for smaller nozzle diameters, and thus higher pressure ratios, it is unknown to what extent the diverging effect of configuration 2 occurs.

However, though configuration 1 is currently not deemed suitable, the deposit pattern induced by the restriction requires further analysis. If the pattern is controllable, to for example a line, potentially it becomes viable for patterning.

Configuration 3 gives the smallest deposition diameter for low nozzle to substrate distances, however the deposits show mainly the micro-aggregate region which is also found in the centre of configuration 1 and 2. The

higher nozzle to substrate distances give wall jet deposit which are not suitable for the deposition of patterns or thin films.

Thus configuration 2 shows the most suitable deposits for patterning, specifically the high pressure ratio for small values of L/d_n. Additionally, the configuration shows a circular deposit shape and shows axial symmetry. These properties make the pattern writing uniform and independent of the writing direction.

6. Line patterns

Configuration 2 with the highest pressure ratio was used to patterns lines to verify the usability. The substrate distance for all lines is $L/d_n = 2$ (deposit shape *C2* in Figure 4). The lines are written with different spark and writing variables to see the performance for direct writing. Figure 12 shows the five written lines and Table 3 gives the corresponding process variables, with v_{write} the writing speed and x the amount of writing sweeps, Q_{per} indicates the percentage of Q_{in} that goes to the deposition process (Q_{dep}). Equation 6 calculates the exposure time (t_e), where the value of 410 is the deposit diameter of the deposit shape *C2*. The exposure time (t_e) is a variable to give an indication of the time of deposition on the centre of the line.

$$t_e = \frac{410\,x}{v_{write}} \tag{6}$$

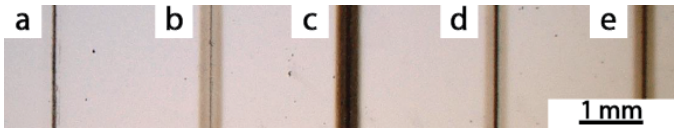

Figure 12: Image of five deposited lines with process variables given by Table 3.

Table 3: Process variables for the five lines indicated in Figure 12

	U_s	I_s	Q_{in}	v_{write}	x	t_e	Q_{per}
	kV	mA	l/min	$\mu m/s$	$-$	s	$\%$
a	1.2	1	0.65	90	8	36.4	15
b	1.2	9	0.65	45	4	36.4	15
c	1.2	9	0.50	90	8	36.4	20
d	1.2	3	0.20	360	20	22.8	50
e	1.2	6	0.20	360	20	22.8	50

6.1. Line analysis

For each line the average is taken of 400 grey scale profiles perpendicular to the write direction. Figure 13 shows the results of the averaged profiles, where the horizontal lines indicate the regions measured with optical microscopy. The measured regions were expected to coincide with different areas in the plot. However, though the different areas are clearly observable in the plots, there is no specific cut-off grey value for each region. This difference is expected to occur due to the subjectivity of the optical measurement.

The centre of the line shows the micro-aggregate region, while outside the region of scattered micro-aggregates and a nanoparticle layer, referred to as the nanoparticle region in the graphs, is visible. Though not indicated in the graphs some of the lines, for example *b* and *e*, show a transition region on the edge where in the optical images the observable particles slowly fade out. These transition regions are related to the rate at which the grey scale decreases in the graphs, and are visible outside the nanoparticle region. Line *a* shows the lowest rate, for which the transition region is barely observed with optical microscopy.

Each of the graphs shows a clear peak at the micro-aggregate region compared to the nanoparticle region. However, graph *a*, *c*, and *e* show two peaks, which indicates the presence of a similar effect seen in the deposits of configuration 2 for the low pressure ratio. In graph *d* the effect is less visible, though the peak consists out of two parts. This is expected to be due to the low current and hence the presence of more microparticles. In Graph *b* the peaks do not show due to a lack of micro-aggregates as a result of the higher flow rate and the higher current. Further details are given in Chapter 4.

Graph *f* shows a comparison of all the lines. It should be noted that it is not a comparison of line thickness, since the grey values are qualitative. However, it compares how the different regions change for the variations in deposition variables. When comparing line *d* and *e*, line *e* shows a lower peak in the micro-aggregate region, but shows a more dense nanoparticle area. In support of this observation, is that the higher current results in a less dense micro-aggregate region. A similar result shows between line *a* and *b*, for which the difference between the density of the micro-aggregate region and nanoparticle region is significant. Line *c* shows the most clear line in optical microscopy and in the graph the line has the widest micro-aggregate region, highest peak value and most clear nanoparticle region. In comparison to line *a* and *b* this observation is a result of the higher amount of evaporated material per volume in addition to the higher amount of Q_{per}. When comparing the line to *d* and *e*, more material than line *a* can be expected due to 50% of Q_{in} available for deposition. However, t_e is significantly lower for line *d* and *e*. This in addition to the higher current, thus higher density in the nanoparticle region, explains the high overall particle density of line *c*.

6.2. Particle analysis

A HR-SEM imaged the regions in the line at higher magnification to gain a better insight on the surface mor-

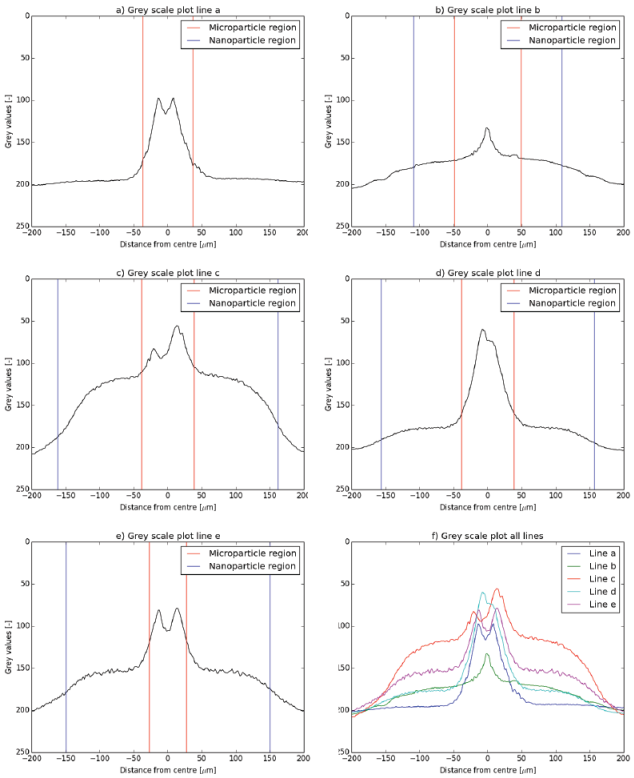

Figure 13: Averaged grey scale values for the deposited lines with horizontal lines indicate the regions that were measured with optical microscopy. Graph f shows each profile in the same graph for comparison. Note that this graph is not used to compare the line thickness's, since the grey values are quantitative results.

phology and primary nanoparticles. Figure 14 shows the micro-aggregate region of lines a to d (i.e. line a is image a).The images are in good agreement with similar images of copper nanoparticles in [26]. Picture c and d shows similarities in the micro-aggregate region, as expected based on the optical microscopy analysis of the lines.

Considering the surface morphology, the particles cover the substrate fully, though not uniformly, by micro-aggregates as suggested by the previously shown SEM images of the deposits. Several big clusters are visible, specifically in b, causing a seemingly rough surface. Image c already shows a less rough surface morphology . Image d, compared to image c, mainly shows a difference in coverage of the substrate. The particles are interconnected but the substrate is not covered completely. One thing that stands out in the images are several, almost perfectly, spherical particles. For each image in Figure 14 the red circle indicates one of them. These are also observed by [26] and they assume these particles are formed by the electrodes releasing liquid material.

Figure 15 depicts HR-SEM images of the micro-aggregates observed in Figure 14. Image d shows that the micro-aggregates are covered in circular shaped primary nanoparticles. In addition, c shows a thread like surface morphology. Images a and b illustrate these thread like structures further. These images conclude that the micro-aggregates that are visible are either complete agglomerates of nanoparticles, or are microparticles covered with layers of these nanoparticle agglomerates.

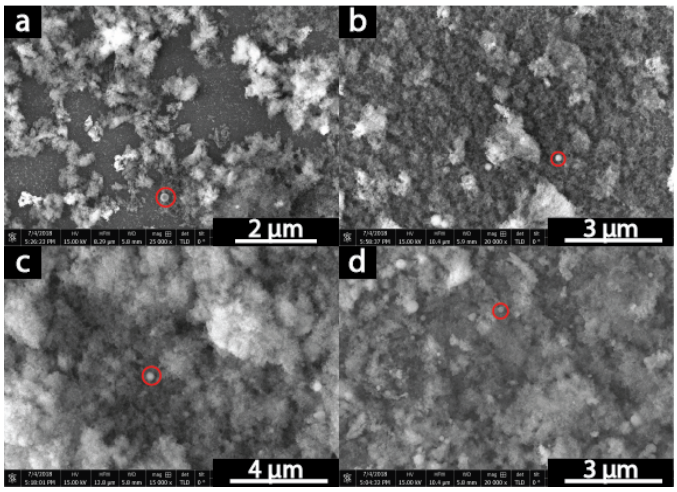

Figure 14: HR-SEM images of the micro-aggregate region of lines a to d, images a to d respectively. The red circle in each picture indicates a spherical particle caused by liquid ejected from the electrodes.

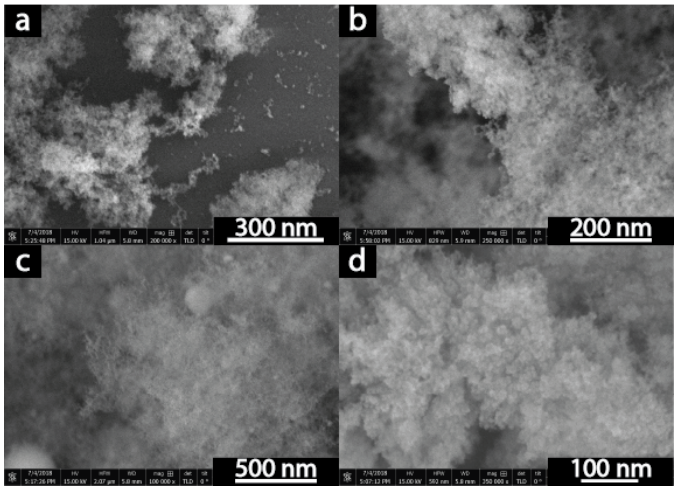

Figure 15: HR-SEM images of the micro-aggregate region of lines a to d, images a to d respectively, at higher magnification than seen in Figure 14.

The edges of lines a to d at low magnification are illustrated in Figure 16. The images confirm that the smaller particles are on the edges as the particle size and particle density decrease perpendicular to the writing direction, most clearly observed in image b and d. The similarities between image b and d was expected due to the similarities between the lines. A minor difference is that image d has a higher particle density. Image c shows the same difference compared to image d. Image a shows the area that is invisible in the normal SEM and a haze in the optical

microscope. The particles in this area are nanoparticles agglomerates and very small compared to those found in the other images. This observation follows the expectation that less material is evaporated with a low current.

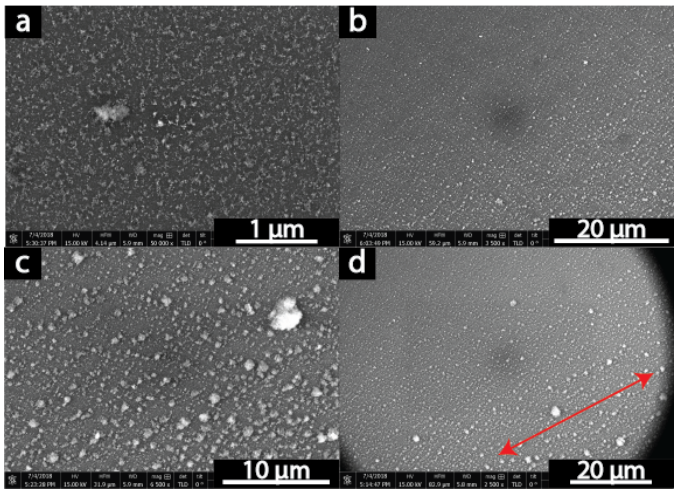

Figure 16: HR-SEM images of the micro-aggregate region of lines a to d, images a to d respectively. The red arrow indicates the writing direction of the lines.

A comparison between the five lines shows clear differences as a result of different deposition variables. For line a and b, with similar t_e, it shows that higher currents cause a more dense nanoparticle region but a less dense micro-aggregate region. Line d and e illustrate the same effect, though the difference in current is smaller. Line c shows an even clearer nanoparticle region than the other lines and has the highest peak in the micro-aggregate region. The HR-SEM images show that the substrate of line c is fully covered for both the regions.

For similar t_e, Q_{per} has a significant influence on the density of the lines, as seen in the comparison between line b and c. This density difference is also visible in the HR-SEM images in micro-aggregate regions, by a rougher surface morphology for line b.

7. Conclusions and recommendations

The sonic configuration with low pressure ratios is deemed to be the most suitable for nanoparticle patterning. The configuration shows a circular deposit with a diameter within two times the nozzle diameter when the substrate is placed close to the nozzle.

With the aerosol consisting of argon and wide size distribution of copper nanoparticle agglomerates, nanoparticle lines were patterned with a width of approximately 400 μm. The patterned lines showed a clear centre region, observed to be micro-sized nanoparticle agglomerates or microparticles covered with a layer of nanoparticles. The nanoparticle region showed scattered micro-aggregates in addition to a uniform nanoparticle layer.

The work shows that patterns can be written with narrow lines. Though narrower lines have been achieved in other works, the system allows for the deposition of nanoparticle lines with different particles sizes without a significant change in line width. For future applications, this allows for a relaxation of the requirements induced by the fabrication process, specifically on the particles in the aerosol.

The lines are characterised by two distinct regions, of which the centre region is expected to be filterable. The deposition variables control the density of each region, and are thus expected to be tunable. By filtering the micro-aggragates, the consistency, and potentially similar functional behaviour over the full line width can be achieved. In addition, by an increase in deposition time, specifically for lower currents, sharp edges are attained for all lines.

Though the system requires further improvements and optimisation steps, the work shows that the system is already capable of patterning nanoparticle lines with different particle sizes. The nanoparticle generator in combination with the deposition configuration allow for a versatile and scalable system. With further research the system can improve on the accessibility of nanoparticle technologies, specifically those involving nanoparticle patterns, to a wider audience.

In conclusion, this work provides a basis for a scalable set-up for the direct writing of nanoparticles. The set-up allows for a wide variety of materials, substrates and particle sizes. Future work could bring these type of set-ups to manufacturing lines that fabricate different types of nanoparticle technologies. With this, nanoparticle technologies become more accessible to industry and thus the consumer market.

References

[1] J. Bravo, L. Zhai, Z. Wu, R. E. Cohen, M. F. Rubner, Transparent superhydrophobic films based on silica nanoparticles, Langmuir 23 (13) (2007) 7293–7298. doi:10.1021/la070159q.

[2] S. Pillai, K. R. Catchpole, T. Trupke, M. A. Green, Surface plasmon enhanced silicon solar cells, Journal of Applied Physics 101 (9). doi:10.1063/1.2734885.

[3] N. A. Isaac, M. Valenti, A. Schmidt-Ott, G. Biskos, Characterization of Tungsten Oxide Thin Films Produced by Spark Ablation for NO2 Gas Sensing, ACS Applied Materials and Interfaces 8 (6) (2016) 3933–3939. doi:10.1021/acsami.5b11078.

[4] B. K. Park, D. Kim, S. Jeong, J. Moon, J. S. Kim, Direct writing of copper conductive patterns by ink-jet printing, Thin Solid Films 515 (19 SPEC. ISS.) (2007) 7706–7711. doi:10.1016/j.tsf.2006.11.142.

[5] K. K. Hon, L. Li, I. M. Hutchings, Direct writing technology-Advances and developments, CIRP Annals - Manufacturing Technology 57 (2) (2008) 601–620. doi:10.1016/j.cirp.2008.09.006.

[6] M. Stoppa, A. Chiolerio, Wearable electronics and smart textiles: A critical review (2014). doi:10.3390/s140711957.

[7] J. M. Hoey, A. Lutfurakhmanov, D. L. Schulz, I. S. Akhatov, A review on aerosol-based direct-write and its applications for microelectronics, Journal of Nanotechnology 2012. doi:10.1155/2012/324380.

[8] D. Hanft, J. Exner, M. Schubert, T. Stöcker, P. Fuierer, R. Moos, An overview of the Aerosol Deposition method: Process fundamentals and new trends in materials applications, Journal of Ceramic Science and Technology 6 (3) (2015) 147–181. doi:10.4416/JCST2015-00018.

[9] J. Akedo, J. Ryu, D.-Y. Jeong, S. Johnson, Chapter 15 – Aerosol Deposition (AD) and Its Applications for Piezoelectric Devices, 2nd Edition, Elsevier Ltd., 2017. doi:10.1016/B978-0-08-102135-4.00015-1.
URL http://dx.doi.org/10.1016/B978-0-08-102135-4.00015-1

[10] P. Piseri, H. V. Tafreshi, P. Milani, Manipulation of nanoparticles in supersonic beams for the production of nanostructured materials, Current Opinion in Solid State and Materials Science 8 (3-4) (2004) 195–202. doi:10.1016/j.cossms.2004.08.002.

[11] J. Fernandez de la Mora, S. Hering, N. Rao, P. McMurry, Hypersonic impaction of ultrafine particles, Journal of Aerosol Science 21 (2) (1990) 169–187. doi:10.1016/0021-8502(90)90002-F.
URL http://linkinghub.elsevier.com/retrieve/pii/002185029090002F

[12] X. Wang, F. E. Kruis, P. H. McMurry, Aerodynamic focusing of nanoparticles: I. Guidelines for designing aerodynamic lenses for nanoparticles, Aerosol Science and Technology 39 (7) (2005) 611–623. doi:10.1080/02786820500181901.

[13] K. S. Lee, S. Kim, D. Lee, Aerodynamic focusing of 5-50 nm nanoparticles in air, Journal of Aerosol Science 40 (12) (2009) 1010–1018. doi:10.1016/j.jaerosci.2009.09.004.
URL http://dx.doi.org/10.1016/j.jaerosci.2009.09.004

[14] L. Zhang, J. Shao, X. Chen, J. Zhang, Q. Si, Design and evaluation of aerodynamic lens system for focusing sub-10 nm nanoparticles, Applied Physics A: Materials Science and Processing 122 (11) (2016) 1–6. doi:10.1007/s00339-016-0489-6.

[15] V. Champagne, D. Helfritch, E. Wienhold, J. DeHaven, Deposition of copper micro-circuitry by capillary focusing, Journal of Micromechanics and Microengineering 23 (6) (2013) 065023. doi:10.1088/0960-1317/23/6/065023.
URL http://stacks.iop.org/0960-1317/23/i=6/a=065023?key=crossref.da152b566a984c46720406d8a5e93b97

[16] R. V. Mallina, A. S. Wexler, M. V. Johnston, High-speed particle beam generation: Simple focusing mechanisms, Journal of Aerosol Science 30 (6) (1999) 719–738. doi:10.1016/S0021-8502(98)00759-9.

[17] T. Walters, Gas-flow Calculations: Don't Choke, Chemical Engineering 107 (1) (2000) 70–76.

[18] O. Abouali, S. Saadabadi, H. Emdad, Numerical investigation of the flow field and cut-off characteristics of supersonic/hypersonic impactors, Journal of Aerosol Science 42 (2) (2011) 65–77. doi:10.1016/j.jaerosci.2010.11.006.
URL http://dx.doi.org/10.1016/j.jaerosci.2010.11.006

[19] O. Abouali, G. Ahmadi, A model for supersonic and hypersonic impactors for nanoparticles, Journal of Nanoparticle Research 7 (1) (2005) 75–88. doi:10.1007/s11051-004-7910-3.

[20] J. Fernández de la Mora, N. Rao, P. McMurry, Inertial impaction of fine particles at moderate reynolds numbers and in the transonic regime with a thin-plate orifice nozzle, Journal of Aerosol Science 21 (7) (1990) 889–909. doi:10.1016/0021-8502(90)90160-Y.
URL http://linkinghub.elsevier.com/retrieve/pii/002185029090160Y

[21] H. Chong, W. T. Nichols, D. T. O'Brien, M. F. Becker, D. Kovar, J. W. Keto, Supersonic jet deposition of silver nanoparticle aerosols: Correlations of impact conditions and film morphologies, Journal of Applied Physics 101 (6). doi:10.1063/1.2710304.

[22] M. Ihalainen, T. Lind, A. Arffman, T. Torvela, J. Jokiniemi, Break-Up and bounce of TiO2 agglomerates by impaction, Aerosol Science and Technology 48 (1) (2014) 31–41. doi:10.1080/02786826.2013.852155.

[23] N. S. Tabrizi, M. Ullmann, V. A. Vons, U. Lafont, A. Schmidt-Ott, Generation of nanoparticles by spark discharge, Journal of Nanoparticle Research 11 (2) (2009) 315–332. doi:10.1007/s11051-008-9407-y.

[24] J. Feng, L. Huang, L. Ludvigsson, M. E. Messing, A. Maisser, G. Biskos, A. Schmidt-Ott, General Approach to the Evolution of Singlet Nanoparticles from a Rapidly Quenched Point Source, Journal of Physical Chemistry C 120 (1) (2016) 621–630. doi:10.1021/acs.jpcc.5b06503.

[25] C. Chiappini, P. Piseri, S. Vinati, P. Milani, Supersonic cluster beam deposition of nanostructured thin films with uniform thickness via continuously graded exposure control, Review of Scientific Instruments 78 (6) (2007) 2005–2008. doi:10.1063/1.2746824.

[26] N. S. Tabrizi, M. Ullmann, V. A. Vons, U. Lafont, A. Schmidt-Ott, Generation of nanoparticles by spark discharge, Vol. 11, 2009. doi:10.1007/s11051-008-9407-y.

4

Additional experiments

This chapter explains several experiments that were part of the set-up development and showed vital information. The experiments also show similar results as those found in the Chapter 3, and are thus compared.

4.1. Experiment performed at a different set-up

An experiment with the sonic deposition configuration (configuration 3) without restriction was performed at VSP. The experiment varies the pressure (p_2) and substrate distance (L) and thus shows similarities with the experiments done for each deposition configuration. A different sonic nozzle was manufactured for the experiments due to the inlet in the vacuum chamber being 6 mm instead of the 10 mm. The nozzle has a choked flow of 0.65 l/min. The experiment consists of nine deposits with three steps for p_2 and L. The results are given in Figure 4.1 with the common deposition variables in the upper left corner. The deposits are named by a letter (columns) and a number (rows).

Three general observations are made based on visual inspection and the knowledge of Chapter 3. Firstly, the deposit shape shows differences with those found in earlier experiments and are attributed to the nozzle manufacturing process. More details are given in section 4.3. Secondly, Fizeau fringes are found in A1, A2, and B1, which indicate a thickness gradient. Thirdly, B3 and C3 have an empty region around the centre of the deposit, which shows similarities with either a less dense inner region or the wall jet deposits.

in Chapter 3, the deposits of the sonic configuration for high pressure ratios ($p_1/p_2 = 100$), had a micro-aggregate region with constant diameter. At a substrate distance (L) slightly before the Mach disk (L_m) wall jets appear radially outward. The lower pressure ratio ($p_1/p_2 = 50$) showed a continuously diverging micro-aggregate region with a less dense inner region, also divergent.

A comparison between the result of Chapter 3 and the results of this experiment, given in Figure 4.1, shows differences. The differences are a result of the lower downstream pressure (p_2) for the experiments at VSP than those in Chapter 3. The main difference is that the deposits show a nanoparticle region around the micro-aggregates. The edge of this nanoparticle region is more dense, and clearly observed for deposits $B3$ and $C3$, where the nanoparticle region separates from the micro-aggregate region. These deposits have p_2 only slightly lower ($p_2 = 9mbar$) than those in the paper ($p_2 = 10mbar$). Hence, the separated nanoparticle region is assumed to be a wall-jet deposit.

However, the wall jet deposits shows a ring instead of the radially outward stripes. This is attributed to the nozzle type, instead of a conical nozzle, the nozzle utilised in these experiments is a thick plate orifice with a depth of 0.50 mm.

In addition to the comparison with results from the paper, the experiment was used to compare between impactor research aiming for the highest nanoparticle collection. In [47] the most suitable substrate distance for nanoparticle collection is given as $0.67L_m$, which is the case for C2 and B3. However, though these deposits could potentially have the most nanoparticles, the deposit shape shows no favourable properties for direct writing, like a small deposit diameter or a dense nanoparticle region. When compared to other de-

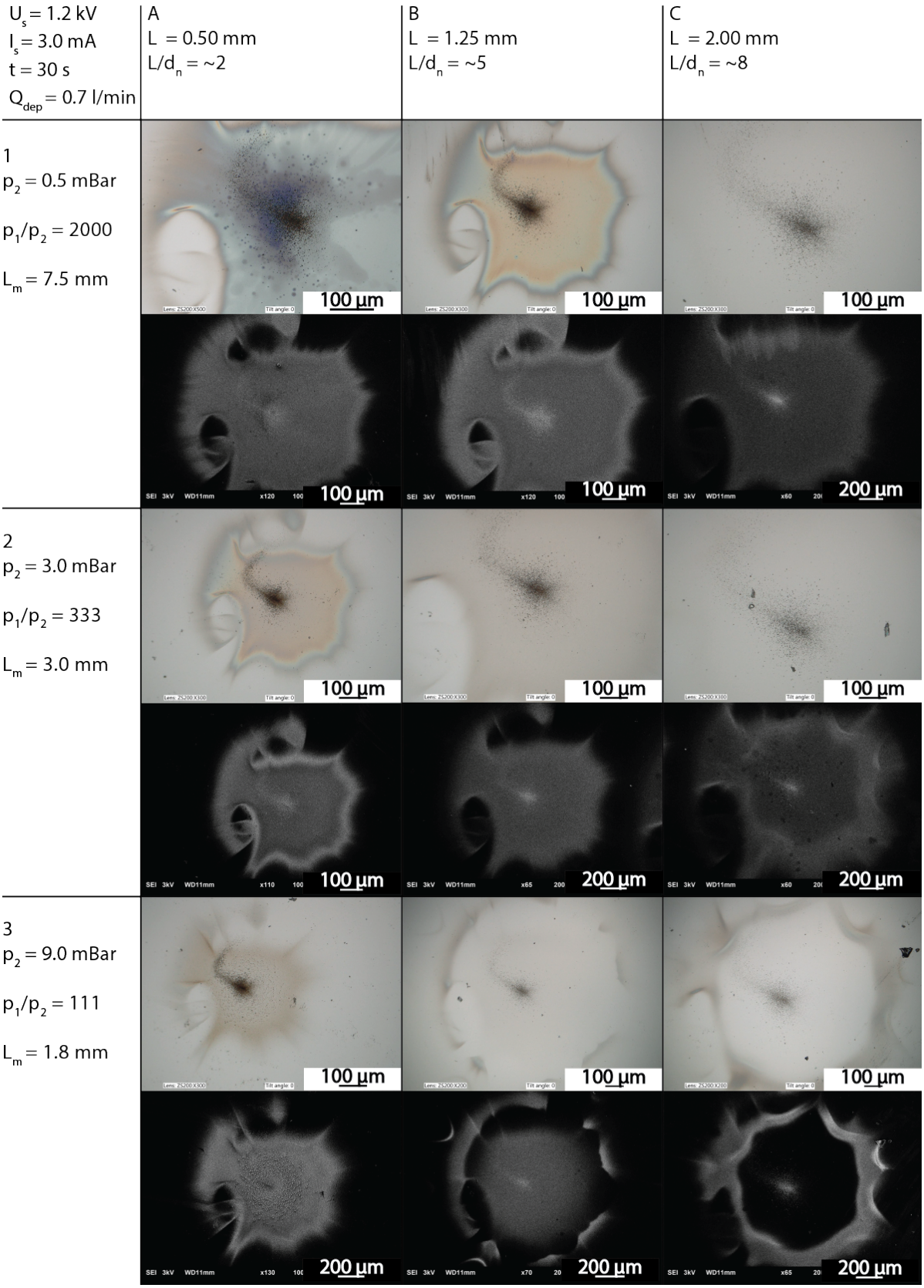

Figure 4.1: Optical and SEM images of nine deposits with variations of substrate distance (X-axis) and vacuum pressure (Y-axis).

posits, specifically the deposits with relatively small L compared to L_m (A1, A2, A3, and B1) show the smallest deposit sizes and most clear nanoparticle regions.

Though the deposits are not favourable for direct writing purposes due to deposit shape and the presence of a denser area on the edges, more nanoparticle agglomerates are present than in Chapter 3 for the same configuration. This observation shows that an improvement to the system to allow for lower pressures, could result in better deposits.

4.2. The influence of vacuum pressure on subsonic deposition

The experiment aims to show how the vacuum pressure influences the deposit for the subsonic configuration. The effect is further examined by a change in spark current (I_s) and the nozzle diameter (1.5 mm and 2.0 mm). Fifteen deposits with 5 variations in p_2 and 3 variations in I_s are made for each nozzle. The common variables are: Q_{in} is 0.5 l/min, Q_{dep} is 0.1 l/min, U_s is 1.2 kV, L is 1 mm and the deposition time is 60 s. The results are given in Figure 4.2 and 4.3 for the 2.0 mm and 1.5 mm nozzle respectively.

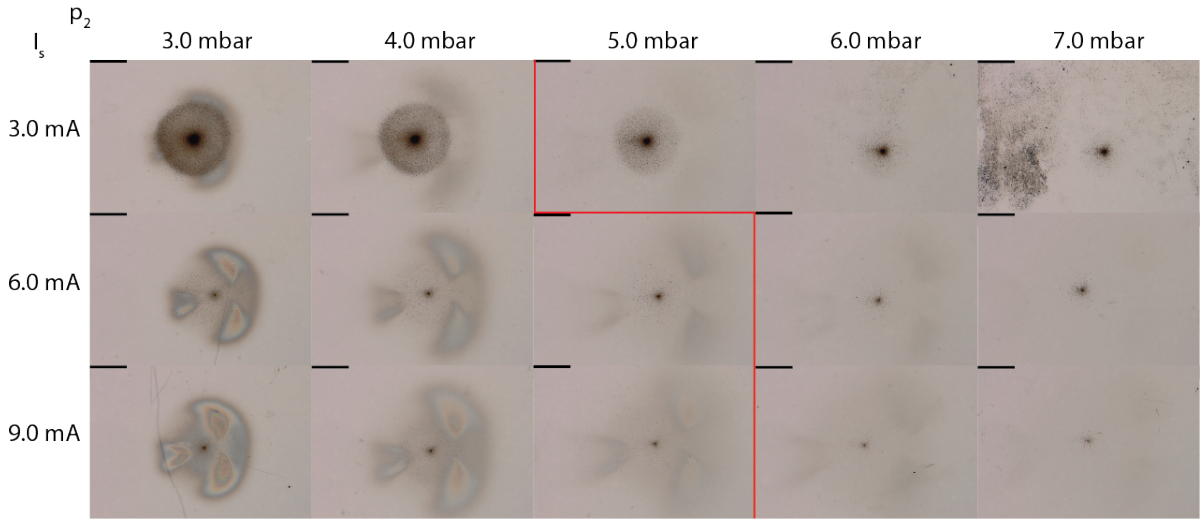

Figure 4.2: Optical microscope images of deposits with varying spark current (I_s) and vacuum pressure levels (p_2). The scale bars in the top left image indicate 0.5 mm and are equal for all deposits. The red line is an indication of what is considered to be the highest pressure at which the nanoparticles agglomerates are deposited. All deposits are made with a nozzle with a throat diameter of 2 mm.

The first thing to note is that both nozzles result in the same deposit pattern, and thus supports the claim made in the paper that the deposit pattern is related to the restriction. The diameter is measured with optical microscopy for several of the deposits, given in Table 4.1. The deposit diameter, which are initially 500 μm less than the nozzle diameter, becomes larger rapidly with increases in p_2. The red line in the figures indicate where the nanoparticle region becomes too vague to be considered as such. For the smaller nozzle, which as a result has a higher velocity subsonic jet, the line is shifted towards higher values of p_2. This illustrates that the higher particle drag is compensated by higher jet velocities. The divergence of the deposit diameter is in contrast with the diameter of the micro-aggregate region, best observed for the deposits with low I_s. The micro-aggregate region is found to converge with an increase in p_2. This is expected to be a result of less acceleration in the nozzle and as a result the micro-aggregates stay focused in the centre-line due to capillary focusing of the tube.

Table 4.1: Deposition diameters in μm of 3.0 and 4.0 $mbar$ deposits.

	2.0 mm nozzle		1.5 mm nozzle		
I_s/p_2	3.0 $mbar$	4.0 $mbar$	3.0 $mbar$	4.0 $mbar$	5.0 $mbar$
3.0 mA	1470	1990	980	1110	1230
6.0 mA	1450	1880	980	1110	1260
9.0 mA	1450	1910	1000	1090	1300

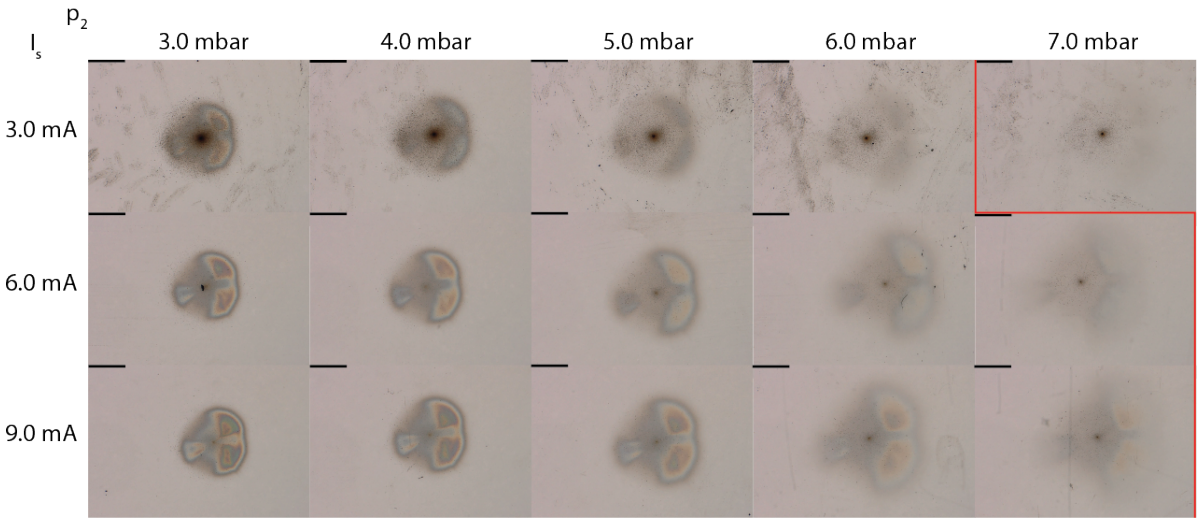

Figure 4.3: Optical microscope images of deposits with varying spark current (I_s) and vacuum pressure levels (p_2). The scale bars in the top left image indicate 0.5 mm and are equal for all deposits. The red line is an indication of what is considered to be the highest pressure at which the nanoparticles agglomerates are deposited. All deposits are made with a nozzle with a throat diameter of 1.5 mm.

The variation in I_s is expected to influence the particles in the aerosol, specifically the particle size. As seen in the paper, higher currents resulted in higher nanoparticle agglomerate densities, while lower currents result in higher micro-aggregate densities. The experiments are in agreement with this result, since the deposits at 3.0 mA show a dense micro-aggregate region, while the nanoparticle region is best observed in the deposits at 9.0 mA. In addition, the lines in the paper showed that the deposit diameter was independent of I_s. The measured diameters of the deposits, given in Table 4.1, show a similar result.

From the experiment it is concluded that the subsonic deposition still requires further investigation in the deposit pattern. The deposit diameter is observed to diverge rapidly for low jet velocities. The deposit diameter is observed to be 500 μm smaller than the nozzle diameter for both experiments, which could indicate that a further reduction of nozzle diameter gets smaller deposit diameters.

4.3. Deposit shapes

The paper already showed a variety of deposit shapes. However, more of them were found throughout this work and resulted in a better understanding of the set-up. The deposit shapes illustrated in Figure 4.4 were created with different nozzles and configurations. Shapes 1 to 3 were made with the sonic configuration without restriction, while 4 is made with the subsonic configuration. The deposition and spark variables for each deposit are given in Table 4.2.

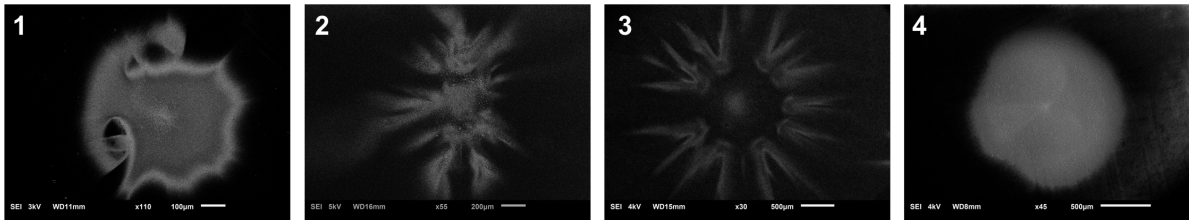

Figure 4.4: Four experiments are done with different configurations (1) sonic deposition with a capillary sonic nozzle for the VSP set-up (2) sonic deposition with a capillary sonic nozzle for the TUDelft setup (3) sonic deposition with a conical nozzle (4) subsonic deposition with Q_A at 0.1 L/min.

The specific deposit shapes seen in 1, 2 and 3 are attributed to nozzle imperfections caused by the fabrication process. This was confirmed by rotating the nozzle and observing a similar rotation in the deposit. Though all three deposits were created with the sonic configuration, the deposit shapes show significant dif-

Table 4.2: Process variables for the four deposits shown in Figure 4.4.

Deposit	L/d_n [-]	p_2 [mbar]	U_s [kV]	I_s [mA]	t [s]
1	2.0	3	1.1	3	60
2	2.0	24	1.1	3	300
3	7.0	10	1.1	3	60
4	1.5	3	1.2	6	60

ferences. Shape 1 is observed to show wall jet deposits for higher values of p_2 (9 $mbar$), as explained in Section 4.1. Shape 3 shows the wall jet deposits at p_2 values of both 10 and 20 $mbar$, see Chapter 3. In the paper the wall jets are closer to the centre for 20 $mbar$. It is therefore expected that the outwards stripes in shape 2 ($p_2 = 24mbar$) are wall jet deposits close to the centre. Deposit shape 4 is related to the restriction. However, no specific reason for the deposit pattern was found.

4.4. The visibility of nanoparticle layers by optical analysis

The deposit patterns are visible with optical microscopy due to the use of a collimated white light beam and the thin layer of nanoparticles. In this section, more detail is given on the coloured deposit patterns as those seen in Figure 4.5. As found in the work of [63], these patterns are visible due to Fizeau fringes. Fizeau fringes are the result of a thickness variation between two reflective layers. The reflections interfere and due to thickness variations the wavelength that interferes changes. For the collimated white light beam, this results in the full visible light spectrum in the deposits.

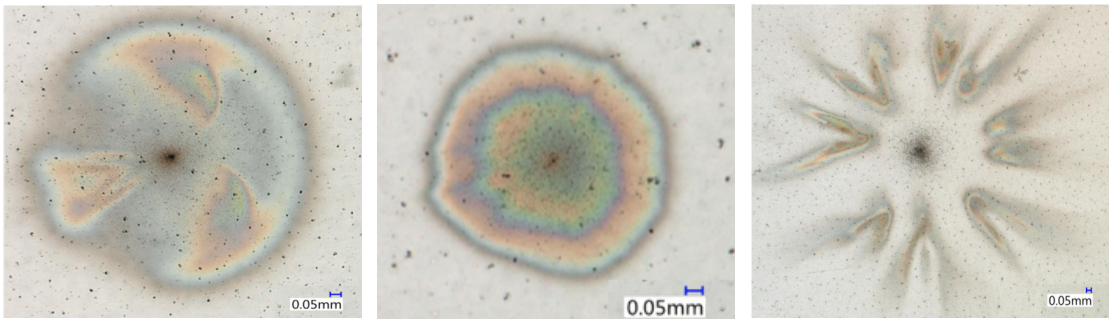

(a) Subsonic deposit which shows colours in a shape as described in Section 4.3

(b) Sonic with critical orifice deposit which shows colour changes in radial direction.

(c) Sonic deposit which shows colour changes in the wall jet deposits.

Figure 4.5: Three different deposits that show Fizeau fringes.

These Fizeau fringes give important information on the thickness of the nanoparticle region. In [63] a rough estimate of 100 nm thickness is given for each full colour spectrum. This could be of interest as initial analysis of the deposits thickness variations. In [64] the Fizeau fringes are used as thickness measurement and compared to a stylus profile meter. The measurements are done on sputter-coated aluminium thin films, and shows that the thickness of thin films between 0.11 and 0.39 μm are measurable with an accuracy within 8 % of the stylus profiler.

However, the thickness between the minimum and maximum values are only measurable relative to other Fizeau fringes. Additionally, the minima and maxima might differ per material due to different optical properties. The direction of the gradient is deduced by the colour order in the deposit. For a thickness increase, the wavelength of the interfering light increases (from blue to red), and vice versa.

Since only limited information is available on Fizeau fringes, an analysis is done on the effect of spark variables on the Fizeau fringes. Configuration 2 was used due to the Fizeau fringes showing radial dependence, and based on the order of the interfering light the thickness decreases radially. Figure 4.6 shows four deposits with different parameters, as given in Table 4.3.

Several similarities are observed in the four deposits. As expected, all of the deposits show the Fizeau

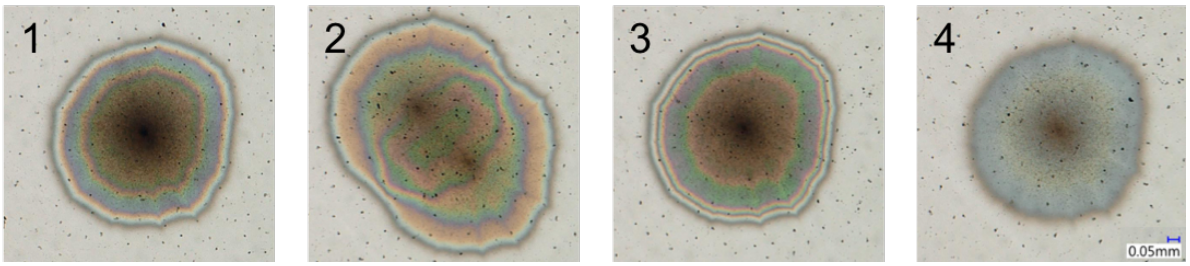

Figure 4.6: Four experiments done to show the influence of several process variables on the deposits. (1) the reference deposit (2) two times the reference deposit slightly shifted (3) increase of deposit time (4) decrease of spark current.

Table 4.3: Process variables for the four deposits shown in Figure 4.6.

Deposit	L/D[-]	p_2 [mbar]	U_s [kV]	I_s [mA]	t [s]
1	3	2.8	1.2	6	60
2	3	2.8	1.2	6	60 + 60
3	3	2.8	1.2	6	120
4	3	2.8	1.2	3	60

fringes and give a similar deposit shape. The diameters of the deposits were measured to be similar, though deposit 4 has a less-defined edge. This is a similar observation as made in Section 4.2, where the spark variables did not influence the deposit size either. Deposit 1 shows approximately 3 repetitions of the visible light spectrum, and based on [63], would indicate a thickness decrease of approximately 300 nm. The first colour observed around the centre is green that turns into blue, with a rapid switch to red. This indicates that the thickness decreases radially outward.

In deposit 2 two deposits overlap and show that the Fizeau fringes change for the intersecting part. The centres of the deposits are identified by the presence of microparticles. Interesting to note is that the interference effect seems symmetric, apparently the surface alterations introduced by the first deposit does not influence the second deposit. Deposit 3 which has twice the normal deposition time shows that the distance between repetitions of the full colour spectrum decrease, specifically observable towards the edges. This could indicate a high thickness gradient at the edges and as a result sharp edges. The decrease of thickness gradient towards the centre shows either that the surface flattens, or is caused by smaller wavelengths not transmitting through the deposit due to the thickness. Deposit 4 which has half the current shows only two Fizeau fringes, blue and green. This is due to less material ablated from the electrodes, thus less material is deposited and the result is a thinner layer.

5

Conclusions

The sonic configuration with low pressure ratios (~24) is found to be the most suitable for direct writing. The used restriction causes a decrease in the upstream pressure and limits the appearance of large radial patterns, as those found for the sonic configuration with a high pressure ratio (~100). The single spot deposits have a circular shape and a deposit diameter of 410 μm which is significantly smaller than those found for the subsonic configuration (1500 μm). Further optimisation of the sonic configuration is expected to result in even smaller deposits. However, additional experiments also showed that further improvements to the experimental set-up make the other configurations more applicable for direct-writing.

The applicability of the configuration was verified by the patterning of lines. The lines are characterised by two regions, the micro-aggregate region and the nanoparticle region. The deposited lines revealed that the density of these regions is influenced by the spark variables. The width of the lines is similar to the deposit diameter, and is independent of the spark variables. This means well-defined edges and a high consistency of the line can be achieved by tuning the spark variables.

In conclusion, the most favourable deposition conditions for the investigated configurations were found and verified to be capable of the direct writing of nanoparticle patterns. With the gained knowledge about the synthesis and deposition process, it is envisioned that other materials can be printed with a similar set-up.

6

Recommendations

6.1. Future work

- **Fizeau fringes**

  The work revealed the appearance of Fizeau fringes in the nanoparticle layers. Research on Fizeau fringes shows that they are caused by interference of the reflections from the nanoparticle layer and the substrate. In future work, the usability of the Fizeau fringes as an on-line monitoring process of the deposit thickness should be investigated.

- **Focus effect related to the restriction**

  For the subsonic configuration, a deposit pattern is found that is related to the restriction. Though the deposit pattern in this work is not usable, a further investigation on the cause of the effect could lead to a more suitable deposit pattern.

- **Wider range of variables**

  The additional experiments show that a further decrease of the downstream pressure can lead to more suitable deposits. Currently, the set-up has a minimum of 3.5 $mbar$ for the configuration with a restriction. Though it is unknown whether lower pressure improve the deposits, the effect of small pressure variations shows large deposit differences, as seen in Section 4.2.

- **Stokes number**

  In this work, the Stokes number was used to illustrate how certain variables influence the deposition variables. Literature suggests that the Stokes number is often determined experimentally, and for future work thus could be done to gain more quantitative results.

6.2. Set-up

- **XYZ-stage**

  The most significant leak in the set-up is caused by the ring seal that allows for movement in Z-direction. Replacing the XY-stage into an XYZ-stage makes a more robust vacuum fitting possible. In addition, a higher stability of the pressure is gained due to the leak rate not being influenced by movement in Z-direction.

- **Restriction**

  Replacing the restriction, though relatively easy, requires the movement of the vacuum chamber. Especially when the more robust vacuum fitting is added, it is required to find a better solution for the replacement of the restriction.

- **Flow controllers**

  Currently, the pressure in the vacuum chamber is controlled by a ball valve that chokes the pumping rate. However, the valve is difficult to control properly and could be replaced by a flow controller.

- **More robust stage**

  The stage is currently set perpendicular to the flow visually, which increases the error on the substrate distance when moving in X-direction. It should be possible to put the stage perpendicular in a more accurate manner. If other angles are required, the stage should allow for actuated rotations.

- **Nozzle improvements**

  The nozzles were made on a manually controlled lathe and are prone to fabrication errors, causing irregularities in the deposits, as seen in Section 4.3. It is recommended to use an automatic lathe for higher precision nozzles.

A

Unique properties and functionalities of nanoparticles

Nanoparticles are objects with dimensions between 1 and 100nm. By reducing the size of the particles the surface to volume ratio increases, which results in property changes. This causes effects, that cannot always be observed at the bulk scale, to be more distinct. Other effects, specifically related to quantum mechanics, are unique to the nanoscale. This gives rise to research and development of applications which utilize such effects. As the nanoparticle fabrication processes develop further and with this the synthesis of nanoparticles becomes more accessible, the field of nanotechnology related to nanoparticles gains an increasing amount of interest.

The changes induced by reduction of the dimensions depend on several aspects: the surface to volume ratio, the material type, and quantum mechanics. This sections explains several effects and property changes which are categorized based on material type dependence. Material type independent properties are observable in all nanoparticles, while the dependent material types are only observable in certain material types.

A.1. Material type independent properties

Changes independent of material type are induced by the surface to volume ratio. This is associated with an increase in the energy required to create new surfaces, more commonly known as the surface energy [65]. A non-exhaustive list of material type independent properties is shown below.

- **Melting-point**; a decrease of the melting point, though increases are reported and caused by the superheating phenomenon. The increases have mostly been reported when nanoparticles are embedded in different materials [66].
- **Stability**; as the surface energy increases, more energy is required to create new surfaces, which in turn can cause materials (like TiO_2) to stop sublimating and become stable as a nanoparticle [65].
- **Diffusivity**; when considering the same mass, smaller particles have a significantly larger surface. This increases interaction between surface and other substances. Nanoparticles are therefore researched for nanofluids [67, 68], catalysis [69] and similar applications.
- **Hardness**; increase of the hardness of a material due to the Hall-Petch effect. However, below a critical size the hardness decreases because of the shear stress which overcomes the friction in the grains [70].

A.2. Material type dependent properties

Material type dependent changes at the nanoscale are caused by both the surface to volume ratio and quantum mechanics. These quantum mechanics effects are caused by discretisation of energy levels as particle sizes reach the wavelength of electrons.

The effects and property changes are subdivided into two categories based on material type: metals, and semiconductors and oxides.

A.2.1. Metals

In metals an effect is observed where the free electron is oscillating in the alternating electric field of light, called Surface Plasmon Resonance (SPR) [71]. As described in [72] additional properties are influenced by the excitation of the electron. To change the susceptibility to different wavelengths, the effect is tuned by the nanoparticles shape, size, and material. [73–75]. For example, the shape and size of nanoparticles, specifically gold and silver, can be tuned to be affected by the wavelengths of visible light. The selection of material results in favourable properties for the application, for instance, gold is researched for in-vivo applications due to its non-reactive nature [74, 76].

By reducing the dimensions of magnetic nanoparticles below a critical size, lower than the single magnetic domain size, changes occur in the magnetic properties as described in [77] and [78]. When additionally the temperature is above a critical value, denoted as the blocking temperature, the material becomes superparamagnetic [79]. Superparamagnetism causes the direction of the dipole moment to switch due to external influences, which results in the net magnetic field to be zero when measured over time [80]. When an external magnetic field is applied, the particles have a fast response and align with the magnetic field. By removal of the external magnetic field, the net magnetic field becomes zero as the particles are not able to retain magnetization [78].

A.2.2. Semiconductors and oxides

The exciton is a state where an electron is excited to the conductance band and forms a bound electron-hole pair [81]. The exciton defines electrical and optical properties of semiconductor materials. The Bohr radius, a material dependent value, determines the size of the exciton. Particles with dimensions less than this radius confine the exciton spatially. This phenomenon is called quantum confinement [82]. Properties of the semiconductor can be tuned by this confinement which is, for instance, used for creating quantum dots [10].

Transducer effects seen in semiconductors, like photovoltaics and piezoelectrics, remain applicable in the nanoparticles. Less significant effects like pyroelectrics, which creates a potential due to temperature fluctuations, become relevant. These effects are researched on the nanoscale as they have the potential to generate energy from otherwise neglected or lost sources, like stress changes or friction losses [15, 16, 20].

B

Investigation of spark variables on evaporated mass

In the set-up development, as described in Chapter 2, a rough estimate was made on the generated mass compared to the deposited mass. The equations for the generated mass were taken from [41]. The generated mass is calculated per spark, which indicates that the spark frequency (f_s) influences the amount of ablated material significantly. However, f_s is a variable that is not measured in the machine, and thus requires a further investigation. Specifically, the influences of the spark variables on f_s.

The VSP G1 allows for two variables to be set, a voltage (U_s) and a current (I_s) and the set-up allows for control over the flow rate (Q_{in}). In addition, the set point of I_s changes the spark frequency (f_s), but the measured current signal does not influence f_s. Equation B.1 gives the relation between these variables, where U_{br} is the breakdown voltage and C is the capacitance of the VSP G1 (20 nF). The breakdown voltage is the voltage at which a spark comes into existence and is calculated by Equation B.2, where U_0 is the voltage difference between U_s and U_{br}, called the overvoltage [30]. Further influences on f_s are investigated, as given in Table B.1. f_s was measured by a sound recording of the process after which the frequency is averaged over 10 seconds.

$$f_s = \frac{I_s}{C\,U_{br}} \tag{B.1}$$

$$U_{br} = U_s + U_0 \tag{B.2}$$

Table B.1: Process variables for the four deposits shown in Figure 4.6.

Id	Q_{in} [l/min]	U_s [kV]	I_s [mA]	f_s [Hz]	U_0 [kV]
1	5.0	1.0	1.0	21.0	1.4
2	5.0	1.3	1.0	15.0	2.0
3	5.0	1.3	2.0	29.0	2.2
4	5.0	1.0	2.0	39.0	1.6
5	2.5	1.0	2.0	40.0	1.5
6	2.5	1.3	2.0	32.0	1.8
7	2.5	1.3	1.0	14.0	2.3
8	2.5	1.0	1.0	18.0	1.8
9	2.5	1.0	0.1	3.5	0.4

From the table, it is observed that both U_s and I_s influence f_s, this is in agreement with Equation B.1. The equation shows that f_s has a proportional dependence on I_s. However, it is observed that the overvoltage also increases with I_s. The small differences of f_s based on Q_{in} is assumed to be due to the instabilities of the spark. The stability of the spark is less for combinations of a low flow rate and high current. The observation in the paper and in Section 4.2 that more micro-aggregates are generated for lower currents, seems to

coincide with the breakdown voltage. It is however unsure, whether this is the actual reason for the higher generation rate.

The rough estimate of Chapter 2 was made by calculating the amount of particles in a deposit of 300 μm. The particles are assumed to be a single layer of 1 μm particles, and cover approximately 80 percent of the deposit area (72000 particles). Compared to the actual deposit, which took 10 minutes of deposition, these approximations are expected to increase the amount of material on the substrate. However, for copper particles, the mass is only 2.7 μg, which is a significant difference compared to the evaporation rates indicated by the VSP-G1 manufacturer (0.1 - 100 mg/h). The equations for generated mass were applied for the deposit variables and the measured frequency, and showed an evaporation rate of approximately 3.4 mg/h.

C

Protocols for operation of the experimental set-up

In this appendix, a more practical step by step guide is given on the operation of the set-up. The appendix consists of three protocols: general operation of the set-up, changing the deposition configuration, and a substrate preparation protocol.

C.1. General operation of the set-up

General comments:

- Whenever equipment is handled which was (possibly) exposed to nanoparticles, wear gloves. This includes anything related to the vacuum chamber.
- Keep the vacuum chamber closed when possible, to prevent contamination of both the environment and the vacuum chamber itself.

C.1.1. Placement of the substrate

1. Verify that all the valves that influence the flow towards the vacuum chamber are closed.
2. Move the nozzle away from the stage by manually turning the knob on the vacuum chamber to control the Z-direction.
3. Open the vacuum chamber and place the substrate in the holder.
4. Close the vacuum chamber.

C.1.2. Deposition

1. Verify that the distributing-plug is switched on.
2. Verify that the Bronckhorst flow-controller, the VSP-G1, the pressure gauge readout, and the stage controller are on.
3. Press ok to align the electrodes of the VSP-G1.
4. Verify that the carrier gas flask is open.
5. Verify that the deposition path and the vacuum chamber vent path are closed, while the waste path is open.
6. Start the vacuum pump by the switch found on the pump itself (verify that the path from pump to vacuum chamber is open).
7. Set the desired pressure by choking the path from pump to vacuum chamber.

8. Set the desired flow rate on the Bronckhorst controller.
9. Set the desired voltage and desired current on the VSP-G1 and press the on button.
10. Set the preferred deposition location by moving the stage.
11. Wait for the measured voltage and current are equal to the set-points. All the generated material leaves the system through the waste path at this point.
12. There are two ways to start the deposition:

    a) Open the deposition path directly. The flow entering the chamber requires the vacuum pressure to stabilise during deposition.

    b) Stop the spark ablation process, wait to ensure no nanoparticles are left in the flow, open the deposition path and wait for the vacuum pressure to stabilise, finally start the spark ablation process again. This ensures that the full deposition occurs at the same pressure level. However, though the spark ablation starts close to the set-point, the RC-circuit is not perfect and requires a short stabilisation period.
13. Close the deposition path (for a) or stop the spark ablation process (for b). If further deposits are needed on the same substrate, start from step 7.

C.1.3. Removal of the substrate

1. Ensure the spark ablation process is stopped.
2. Keep the deposition path open for approximately 2 minutes to flush the vacuum chamber of any loose particles.
3. Close the deposition path.
4. Set the Bronkhorst controller to 0.
5. Close the waste path.
6. Turn off the vacuum pump.
7. Open the vent channel to bring the vacuum chamber to atmospheric pressure.
8. Verify that all the valves that influence the flow towards the vacuum chamber are closed.
9. Move the nozzle away from the stage by manually turning the knob on the vacuum chamber to control the Z-direction.
10. Open the vacuum chamber and take the substrate from the holder.
11. Close the vacuum chamber.

C.2. Change of the deposition configuration

Figure C.1 shows the schematic and the location of the restriction. The restriction is replaced by removing both threaded sockets and pushing the whole tubing into the vacuum chamber. Two things to note in this process are:

- The stage is shifted back to allow for enough room to push the tubing.
- All valves are open to prevent slight pressure differences. It was noted that this causes the tubing to be sucked into the vacuum chamber.

The nozzles are clamp fitting, and are thus replaced by opening the vacuum chamber and pushing on a new nozzle. However, for this process there are three things to take into account:

- The stage is shifted back to allow for enough room to push the nozzle onto the tubing.

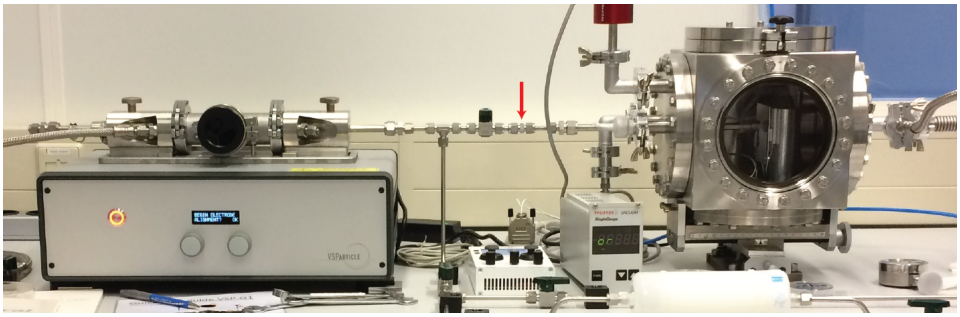

Figure C.1: The experimental set-up where the location of the restriction is indicated by the red arrow

- The nozzle is clamped properly, specifically for the sonic configuration without restriction. The pressure difference can cause a force that propels the nozzle of the tubing.
- Not properly clamped nozzles are clamped by a piece of Teflon. Do not use sticky tape for this process since it corrodes the aluminium tubing.

D

Supplemental figures

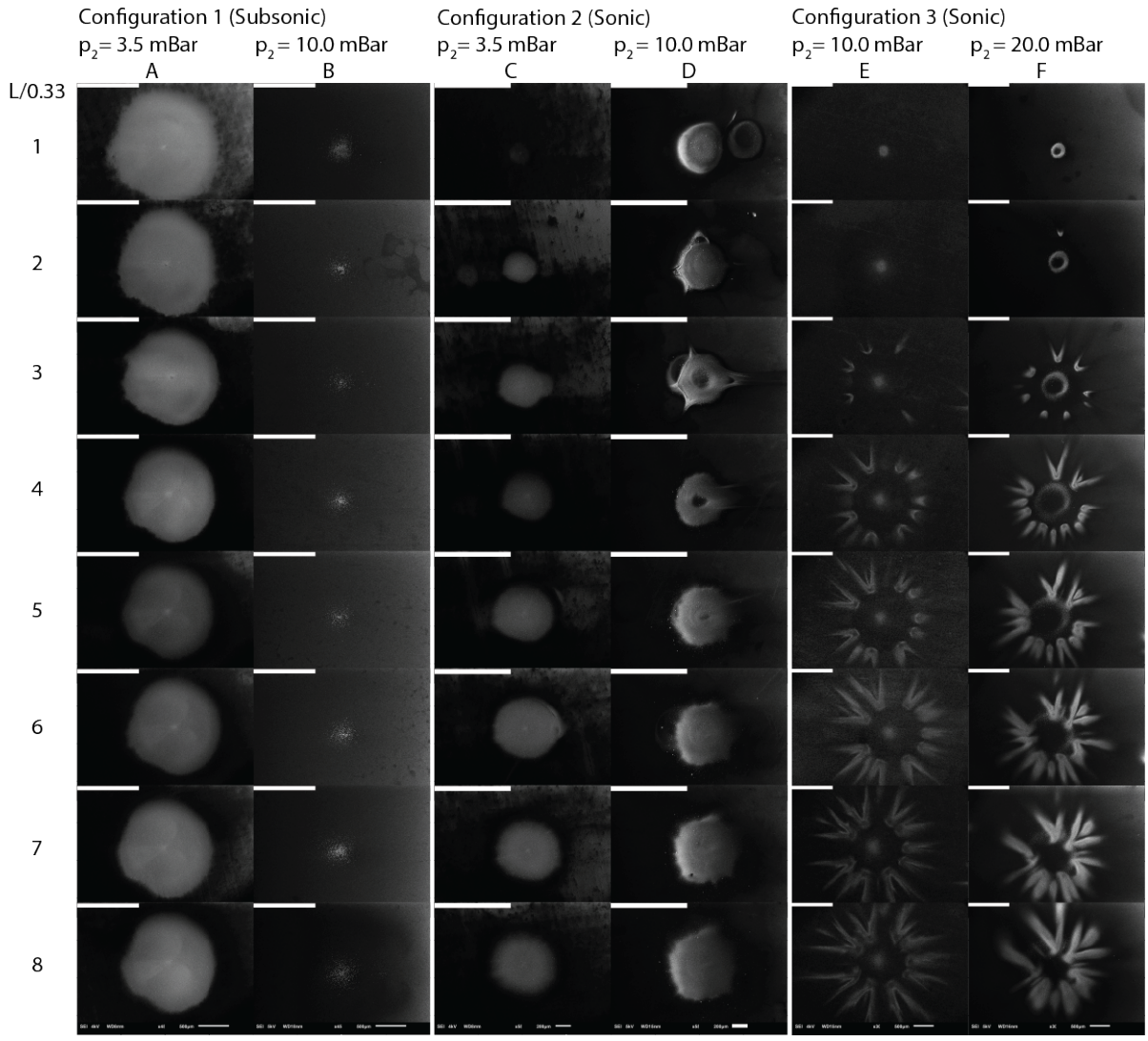

Figure D.1: Larger version of the SEM table.

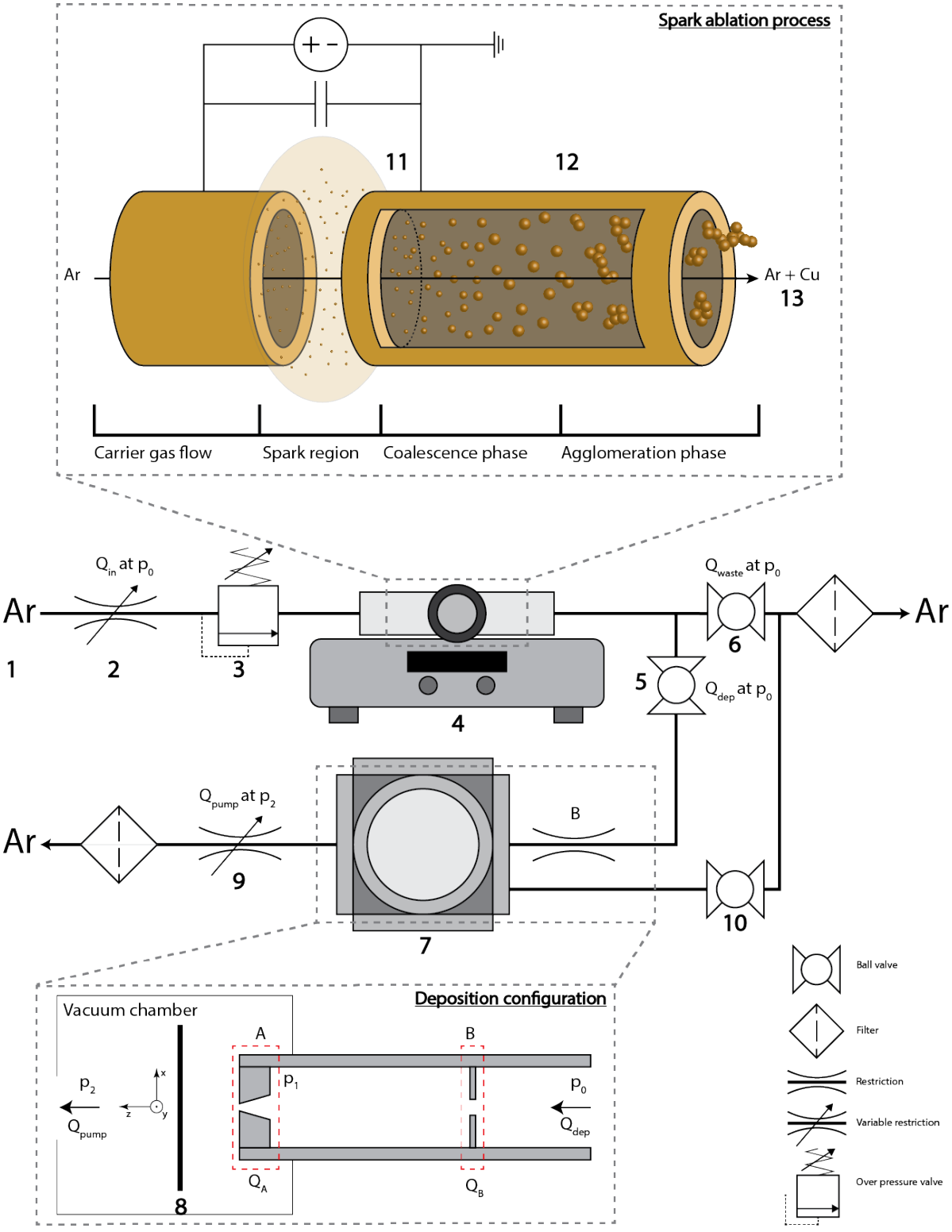

Figure D.2: Larger version of the set-up schematic.

Bibliography

[1] Florian J. Heiligtag and Markus Niederberger. The fascinating world of nanoparticle research. *Materials Today*, 16(7-8):262–271, 2013. ISSN 13697021. doi: 10.1016/j.mattod.2013.07.004. URL http://dx.doi.org/10.1016/j.mattod.2013.07.004.

[2] Steven L. Girshick. Aerosol processing for nanomanufacturing. *Journal of Nanoparticle Research*, 10(6): 935–945, 2008. ISSN 13880764. doi: 10.1007/s11051-007-9331-6.

[3] Bong Kyun Park, Dongjo Kim, Sunho Jeong, Jooho Moon, and Jang Sub Kim. Direct writing of copper conductive patterns by ink-jet printing. *Thin Solid Films*, 515(19 SPEC. ISS.):7706–7711, 2007. ISSN 00406090. doi: 10.1016/j.tsf.2006.11.142.

[4] Nishchay A. Isaac, Marco Valenti, Andreas Schmidt-Ott, and George Biskos. Characterization of Tungsten Oxide Thin Films Produced by Spark Ablation for NO2 Gas Sensing. *ACS Applied Materials and Interfaces*, 8(6):3933–3939, 2016. ISSN 19448252. doi: 10.1021/acsami.5b11078.

[5] K. K.B. Hon, L. Li, and I. M. Hutchings. Direct writing technology-Advances and developments. *CIRP Annals - Manufacturing Technology*, 57(2):601–620, 2008. ISSN 00078506. doi: 10.1016/j.cirp.2008.09.006.

[6] Matteo Stoppa and Alessandro Chiolerio. Wearable electronics and smart textiles: A critical review, 2014. ISSN 14248220.

[7] Justin M. Hoey, Artur Lutfurakhmanov, Douglas L. Schulz, and Iskander S. Akhatov. A review on aerosol-based direct-write and its applications for microelectronics. *Journal of Nanotechnology*, 2012, 2012. ISSN 16879503. doi: 10.1155/2012/324380.

[8] William C. Hinds. Aerosol Technology Properties, Behavior, and Measurement of Airborne Particles. *Journal of Aerosol Science*, 31(9):1121–1122, sep 2000. ISSN 00218502. doi: 10.1016/S0021-8502(99)00571-6. URL http://linkinghub.elsevier.com/retrieve/pii/S0021850299005716.

[9] A. J. Nozik, M. C. Beard, J. M. Luther, M. Law, R. J. Ellingson, and J. C. Johnson. Semiconductor quantum dots and quantum dot arrays and applications of multiple exciton generation to third-generation photovoltaic solar cells. *Chemical Reviews*, 110(11):6873–6890, 2010. ISSN 00092665. doi: 10.1021/cr900289f.

[10] P V Kamat. Quantum Dot Solar Cells. Semiconductor Nanocrystals as Light Harvesters. *Journal of Physical Chemistry C*, 112(48):18737–18753, 2008. ISSN 1932-7447. doi: 10.1021/jp806791s.

[11] S. Pillai, K. R. Catchpole, T. Trupke, and M. A. Green. Surface plasmon enhanced silicon solar cells. *Journal of Applied Physics*, 101(9), 2007. ISSN 00218979. doi: 10.1063/1.2734885.

[12] Maja Gajic, Fabio Lisi, Nicholas Kirkwood, Trevor A. Smith, Paul Mulvaney, and Gary Rosengarten. Circular luminescent solar concentrators. *Solar Energy*, 150:30–37, 2017. ISSN 0038092X. doi: 10.1016/j.solener.2017.04.034. URL http://dx.doi.org/10.1016/j.solener.2017.04.034.

[13] Daan A van den Ende, Wilhelm A Groen, and Sybrand van der Zwaag. Robust piezoelectric composites for energy harvesting in high-strain environments. *Journal of Intelligent Material Systems and Structures*, 24(18):2262–2269, 2013. ISSN 1045-389X. doi: 10.1177/1045389X12462646. URL http://journals.sagepub.com/doi/10.1177/1045389X12462646.

[14] So Young Kim, Sangsik Park, Han Wool Park, Do Hyung Park, Youngjin Jeong, and Do Hwan Kim. Highly Sensitive and Multimodal All-Carbon Skin Sensors Capable of Simultaneously Detecting Tactile and Biological Stimuli. *Advanced Materials*, 27(28):4178–4185, 2015. ISSN 15214095. doi: 10.1002/adma.201501408.

[15] Brijesh Kumar and Sang Woo Kim. Energy harvesting based on semiconducting piezoelectric ZnO nanostructures. *Nano Energy*, 1(3):342–355, 2012. ISSN 22112855. doi: 10.1016/j.nanoen.2012.02.001. URL http://dx.doi.org/10.1016/j.nanoen.2012.02.001.

[16] Ran Ding, He Liu, Xiaoli Zhang, Juanxiu Xiao, Rahul Kishor, Huaxi Sun, Bowen Zhu, Geng Chen, Fei Gao, Xiaohua Feng, Jingsheng Chen, Xiaodong Chen, Xiaowei Sun, and Yuanjin Zheng. Flexible Piezoelectric Nanocomposite Generators Based on Formamidinium Lead Halide Perovskite Nanoparticles. *Advanced Functional Materials*, 26(42):7708–7716, 2016. ISSN 16163028. doi: 10.1002/adfm.201602634.

[17] Gang Cheng, Zong Hong Lin, Long Lin, Zu Liang Du, and Zhong Lin Wang. Pulsed nanogenerator with huge instantaneous output power density. *ACS Nano*, 7(8):7383–7391, 2013. ISSN 19360851. doi: 10.1021/nn403151t.

[18] Jie Chen, Hengyu Guo, Xianming He, Guanlin Liu, Yi Xi, Haofei Shi, and Chenguo Hu. Enhancing Performance of Triboelectric Nanogenerator by Filling High Dielectric Nanoparticles into Sponge PDMS Film. *ACS Applied Materials and Interfaces*, 8(1):736–744, 2016. ISSN 19448252. doi: 10.1021/acsami.5b09907.

[19] Zhong Lin Wang. Triboelectric nanogenerators as new energy technology and self-powered sensors – Principles, problems and perspectives. *Faraday Discuss.*, 176(Xx):447–458, 2014. ISSN 1359-6640. doi: 10.1039/C4FD00159A. URL http://xlink.rsc.org/?DOI=C4FD00159A.

[20] Ya Yang, Wenxi Guo, Ken C Pradel, Guang Zhu, Yusheng Zhou, Yan Zhang, Youfan Hu, Long Lin, and Zhong Lin Wang. Pyroelectric nanogenerators for harvesting thermoelectric energy. *Nano Letters*, 12(6):2833–2838, 2012. ISSN 15306984. doi: 10.1021/nl3003039.

[21] H. Ferkel and B. L. Mordike. Magnesium strengthened by SiC nanoparticles. *Materials Science and Engineering A*, 298(1-2):193–199, 2001. ISSN 09215093. doi: 10.1016/S0921-5093(00)01283-1.

[22] Emmanuel P. Giannelis. Polymer-layered silicate nanocomposites: Synthesis, properties and applications. *Applied Organometallic Chemistry*, 12(10-11):675–680, 1998. ISSN 0268-2605. doi: 10.1002/(SICI)1099-0739(199810/11)12:10/11<675::AID-AOC779>3.0.CO;2-V. URL http://deepblue.lib.umich.edu/handle/2027.42/38308.

[23] Naoji Matsuhisa, Daishi Inoue, Peter Zalar, Hanbit Jin, Yorishige Matsuba, Akira Itoh, Tomoyuki Yokota, Daisuke Hashizume, and Takao Someya. Printable elastic conductors by in situ formation of silver nanoparticles from silver flakes. *Nature Materials*, 16(8):834–840, 2017. ISSN 1476-1122. doi: 10.1038/nmat4904. URL http://www.nature.com/doifinder/10.1038/nmat4904.

[24] Walid A. Daoud, John H. Xin, and Yi He Zhang. Surface functionalization of cellulose fibers with titanium dioxide nanoparticles and their combined bactericidal activities. *Surface Science*, 599(1-3):69–75, 2005. ISSN 00396028. doi: 10.1016/j.susc.2005.09.038.

[25] Kevin C Krogman, Thad Druffel, and Mahendra K Sunkara. Anti-reflective optical coatings incorporating nanoparticles. *Nanotechnology*, 16(7):S338–S343, 2005. ISSN 0957-4484. doi: 10.1088/0957-4484/16/7/005. URL http://stacks.iop.org/0957-4484/16/i=7/a=005?key=crossref.1fe1a3eef1f60777c38934dcfbf04ce8.

[26] Zhenyu Wang, Enhou Han, and Wei Ke. Effect of nanoparticles on the improvement in fire-resistant and anti-ageing properties of flame-retardant coating. *Surface and Coatings Technology*, 200(20-21):5706–5716, 2006. ISSN 02578972. doi: 10.1016/j.surfcoat.2005.08.102.

[27] Javier Bravo, Lei Zhai, Zhizhong Wu, Robert E. Cohen, and Michael F. Rubner. Transparent superhydrophobic films based on silica nanoparticles. *Langmuir*, 23(13):7293–7298, 2007. ISSN 07437463. doi: 10.1021/la070159q.

[28] Rik Brydson, Graham Leggett, Richard Jones, David Mowbray, and Iain Todd. *Nanoscale science and technology*. John Wiley & Sons, Ltd, 2005. ISBN 0470850868.

[29] Andrey Voloshko, Jean Philippe Colombier, and Tatiana E. Itina. Comparison of laser ablation with spark discharge techniques used for nanoparticle production. *Applied Surface Science*, 336:143–149, 2015. ISSN 01694332. doi: 10.1016/j.apsusc.2014.10.077. URL http://dx.doi.org/10.1016/j.apsusc.2014.10.077.

[30] N. S. Tabrizi, M. Ullmann, V. A. Vons, U. Lafont, and A. Schmidt-Ott. Generation of nanoparticles by spark discharge. *Journal of Nanoparticle Research*, 11(2):315–332, 2009. ISSN 13880764. doi: 10.1007/s11051-008-9407-y.

[31] Robert E. Newnham. *Properties of Materials | Anistropy | Symmetry | Structure*. Oxford university press, 1 edition, 2005. ISBN 0198520751.

[32] Vincent A. Vons, Louis C P M De Smet, David Munao, Alper Evirgen, Erik M. Kelder, and Andreas Schmidt-Ott. Silicon nanoparticles produced by spark discharge. *Journal of Nanoparticle Research*, 13 (10):4867–4879, 2011. ISSN 13880764. doi: 10.1007/s11051-011-0466-0.

[33] D. A. Mylnikov, A. A. Lizunova, A. A. Efimov, and V. V. Ivanov. Investigation of partially oxidized Ge and Si nanoparticles produced in repetitive pulsed gas discharge. *AIP Conference Proceedings*, 1858:1–5, 2017. ISSN 15517616. doi: 10.1063/1.4989947.

[34] A. Mohan, F.D. Tichelaar, M. Kaiser, M.A. Verheijen, R.E.I. Schropp, and J.K. Rath. Gas phase grown silicon germanium nanocrystals. *Chemical Physics Letters*, 661:185–190, 2016. ISSN 00092614. doi: 10.1016/j.cplett.2016.08.066. URL http://dx.doi.org/10.1016/j.cplett.2016.08.066.

[35] N. S. Tabrizi, Q. Xu, N. M. Van Der Pers, U. Lafont, and A. Schmidt-Ott. Synthesis of mixed metallic nanoparticles by spark discharge. *Journal of Nanoparticle Research*, 11(5):1209–1218, 2009. ISSN 13880764. doi: 10.1007/s11051-008-9568-8.

[36] Bengt O. Meuller, Maria E. Messing, David L J Engberg, Anna M. Jansson, Linda I M Johansson, Susanne M. Norlén, Nina Tureson, and Knut Deppert. Review of spark discharge generators for production of nanoparticle aerosols. *Aerosol Science and Technology*, 46(11):1256–1270, 2012. ISSN 02786826. doi: 10.1080/02786826.2012.705448.

[37] Martin Slotte and Ron Zevenhoven. Energy efficiency and scalability of metallic nanoparticle production using arc/spark discharge. *Energies*, 10(10):1–19, 2017. ISSN 19961073. doi: 10.3390/en10101605.

[38] A. A. Efimov, V. V. Ivanov, A. V. Bagazeev, I. V. Beketov, I. A. Volkov, and S. V. Shcherbinin. Generation of aerosol nanoparticles by the multi-spark discharge generator. *Technical Physics Letters*, 39(12):1053–1056, 2013. ISSN 1063-7850. doi: 10.1134/S1063785013120067. URL http://link.springer.com/10.1134/S1063785013120067.

[39] Jeong Hoon Byeon, Jae Hong Park, and Jungho Hwang. Spark generation of monometallic and bimetallic aerosol nanoparticles. 39:888–896, 2008. doi: 10.1016/j.jaerosci.2008.05.006.

[40] R. Massarczyk, P. Chu, C. Dugger, S. R. Elliott, K. Rielage, and W. Xu. Paschen's law studies in cold gases. *Journal of Instrumentation*, 12(6), 2017. ISSN 17480221. doi: 10.1088/1748-0221/12/06/P06019.

[41] Jicheng Feng, Luyi Huang, Linus Ludvigsson, Maria E. Messing, Anne Maisser, George Biskos, and Andreas Schmidt-Ott. General Approach to the Evolution of Singlet Nanoparticles from a Rapidly Quenched Point Source. *Journal of Physical Chemistry C*, 120(1):621–630, 2016. ISSN 19327455. doi: 10.1021/acs.jpcc.5b06503.

[42] Dongjoon Lee, Kiwoong Lee, Dae Seong Kim, Jong-Kwon Lee, Sei Jin Park, and Mansoo Choi. Hydrogen-assisted spark discharge generation of highly crystalline and surface-passivated silicon nanoparticles. *Journal of Aerosol Science*, 114(February):139–145, 2017. ISSN 00218502. doi: 10.1016/j.jaerosci.2017.09.007. URL http://linkinghub.elsevier.com/retrieve/pii/S0021850217300745.

[43] Huang Chong, William T. Nichols, Daniel T. O'Brien, Michael F. Becker, Desiderio Kovar, and John W. Keto. Supersonic jet deposition of silver nanoparticle aerosols: Correlations of impact conditions and film morphologies. *Journal of Applied Physics*, 101(6), 2007. ISSN 00218979. doi: 10.1063/1.2710304.

[44] Alexey Efimov, Gleb Potapov, Anton Nisan, Maxim Urazov, and Victor Ivanov. Application of the spark discharge generator for solvent-free aerosol jet printing. *Oriental Journal of Chemistry*, 33(2):1047–1050, 2017. ISSN 22315039. doi: 10.13005/ojc/330264.

[45] D. Hanft, J. Exner, M. Schubert, T. Stöcker, P. Fuierer, and R. Moos. An overview of the Aerosol Deposition method: Process fundamentals and new trends in materials applications. *Journal of Ceramic Science and Technology*, 6(3):147–181, 2015. ISSN 21909385. doi: 10.4416/JCST2015-00018.

[46] M. W. Lee, J. J. Park, D. Y. Kim, S. S. Yoon, H. Y. Kim, D. H. Kim, S. C. James, S. Chandra, Thomas Coyle, J. H. Ryu, W. H. Yoon, and D. S. Park. Optimization of supersonic nozzle flow for titanium dioxide thin-film coating by aerosol deposition. *Journal of Aerosol Science*, 42(11):771–780, 2011. ISSN 00218502. doi: 10.1016/j.jaerosci.2011.07.006. URL http://dx.doi.org/10.1016/j.jaerosci.2011.07.006.

[47] Omid Abouali, Saeideh Saadabadi, and Homayoon Emdad. Numerical investigation of the flow field and cut-off characteristics of supersonic/hypersonic impactors. *Journal of Aerosol Science*, 42(2):65–77, 2011. ISSN 00218502. doi: 10.1016/j.jaerosci.2010.11.006. URL http://dx.doi.org/10.1016/j.jaerosci.2010.11.006.

[48] V. V. Golub and Yu. V. Polezhaev. Jets. In *A-to-Z Guide to Thermodynamics, Heat and Mass Transfer, and Fluids Engineering*. Begellhouse. doi: 10.1615/AtoZ.j.jets. URL http://www.thermopedia.com/content/903/.

[49] Dariusz Góral, Franciszek Kluza, and Katarzyna Kozłowicz. Assessment of Heat Transfer and Mass Change During Fruits and Vegetables Impingement Pre-Cooling. *International Journal of Food Engineering*, 10(1):51900914, jan 2014. ISSN 2194-5764. doi: 10.1515/ijfe-2013-0020. URL https://www.degruyter.com/view/j/ijfe.2014.10.issue-1/ijfe-2013-0020/ijfe-2013-0020.xml.

[50] Luis De Juan and J. Fernández De La Mora. Sizing nanoparticles with a focusing impactor: Effect of the collector size. *Journal of Aerosol Science*, 29(5-6):589–599, 1998. ISSN 00218502. doi: 10.1016/S0021-8502(97)10045-3.

[51] P. Piseri, H. Vahedi Tafreshi, and P. Milani. Manipulation of nanoparticles in supersonic beams for the production of nanostructured materials. *Current Opinion in Solid State and Materials Science*, 8(3-4):195–202, 2004. ISSN 13590286. doi: 10.1016/j.cossms.2004.08.002.

[52] J. Fernández de la Mora, Nagaraja Rao, and P.H. McMurry. Inertial impaction of fine particles at moderate reynolds numbers and in the transonic regime with a thin-plate orifice nozzle. *Journal of Aerosol Science*, 21(7):889–909, jan 1990. ISSN 00218502. doi: 10.1016/0021-8502(90)90160-Y. URL http://linkinghub.elsevier.com/retrieve/pii/002185029090160Y.

[53] Nan Zhang, Amit Srivastava, Brendan Kirwan, Alberto Piqué, Raymond C Y Auyeung, Heungsoo Kim, Hae-sung Yoon, Ki-hwan Jang, Eunseob Kim, and Hyun-taek Lee. Hybrid 3D printing by bridging micro / nano processes. 2017.

[54] Xiaoliang Wang, Frank Einar Kruis, and Peter H. McMurry. Aerodynamic focusing of nanoparticles: I. Guidelines for designing aerodynamic lenses for nanoparticles. *Aerosol Science and Technology*, 39(7):611–623, 2005. ISSN 02786826. doi: 10.1080/02786820500181901.

[55] Kwang Sung Lee, Songkil Kim, and Donggeun Lee. Aerodynamic focusing of 5-50 nm nanoparticles in air. *Journal of Aerosol Science*, 40(12):1010–1018, 2009. ISSN 00218502. doi: 10.1016/j.jaerosci.2009.09.004. URL http://dx.doi.org/10.1016/j.jaerosci.2009.09.004.

[56] Lianhua Zhang, Jianxiong Shao, Ximeng Chen, Jingxiang Zhang, and Qingzong Si. Design and evaluation of aerodynamic lens system for focusing sub-10 nm nanoparticles. *Applied Physics A: Materials Science and Processing*, 122(11):1–6, 2016. ISSN 14320630. doi: 10.1007/s00339-016-0489-6.

[57] S Agarwala, G L Goh, W Y Yeong, Roberto S Aga, Eric B Kreit, and Steven R Dooley. Study of aerosol jet printing with dry nanoparticles synthesized by spark discharge. *J. Phys. Series: Journal of Physics: Conf. Series*, 917:1–5, 2017. ISSN 17426596. doi: 10.1088/1742-6596/917/9/092020. URL http://iopscience.iop.org/article/10.1088/1742-6596/917/9/092020/pdf.

[58] Alexey A. Efimov, Gleb N. Potapov, Anton V. Nisan, and Victor V. Ivanov. Controlled focusing of silver nanoparticles beam to form the microstructures on substrates. *Results in Physics*, 7:440–443, 2017. ISSN 22113797. doi: 10.1016/j.rinp.2016.12.052. URL https://doi.org/10.1016/j.rinp.2016.12.052.

[59] Victor Champagne, Dennis Helfritch, Erik Wienhold, and Jennifer DeHaven. Deposition of copper micro-circuitry by capillary focusing. *Journal of Micromechanics and Microengineering*, 23(6): 065023, 2013. ISSN 0960-1317. doi: 10.1088/0960-1317/23/6/065023. URL http://stacks.iop.org/0960-1317/23/i=6/a=065023?key=crossref.da152b566a984c46720406d8a5e93b97.

[60] Ramakrishna V. Mallina, Anthony S. Wexler, and Murray V. Johnston. High-speed particle beam generation: Simple focusing mechanisms. *Journal of Aerosol Science*, 30(6):719–738, 1999. ISSN 00218502. doi: 10.1016/S0021-8502(98)00759-9.

[61] Saeideh Saadabadi, Omid Abouali, Homayoon Emdad, and Goodarz Ahmadi. Investigation of the effect of nozzle shape on supersonic/hypersonic impactors designed for size discrimination of nanoparticles. *Particuology*, 16:60–68, 2014. ISSN 16742001. doi: 10.1016/j.partic.2013.11.009. URL http://dx.doi.org/10.1016/j.partic.2013.11.009.

[62] J. Fernandez de la Mora, S.V. Hering, N. Rao, and P.H. McMurry. Hypersonic impaction of ultrafine particles. *Journal of Aerosol Science*, 21(2):169–187, jan 1990. ISSN 00218502. doi: 10.1016/0021-8502(90)90002-F. URL http://linkinghub.elsevier.com/retrieve/pii/002185029090002F.

[63] C. Chiappini, P. Piseri, S. Vinati, and P. Milani. Supersonic cluster beam deposition of nanostructured thin films with uniform thickness via continuously graded exposure control. *Review of Scientific Instruments*, 78(6):2005–2008, 2007. ISSN 00346748. doi: 10.1063/1.2746824.

[64] Jittima Kongsakul, Nirun Witit-anun, Surasing Chaiyakun, and Pakorn Kaewtrakulpong. Measurement of Aluminum Thin Film Thickness by Fizeau Interferometer Technique. (1).

[65] Ma José Arcos Fernández-garcia and Rodriguez. Metal Oxide Nanoparticles. *Nanomaterials: Inorganic and Bioinorganic Perspectives*, (October):60, 2007. ISSN 1552-9924. doi: 10.1002/0470862106.ia377. URL http://www0.bnl.gov/isd/documents/41042.pdf.

[66] K. K. Nanda. Size-dependent melting of nanoparticles: Hundred years of Thermodynamic model. *Pramana - Journal of Physics*, 72(4):617–628, 2009. ISSN 03044289. doi: 10.1007/s12043-009-0055-2.

[67] Y Xuan and Q Li. Heat transfer enhancement of nanofluids. *International Journal of heat and fluid flow*, 21(1):58–64, 2000. ISSN 0142727X. doi: 10.1016/S0142-727X(99)00067-3. URL http://www.sciencedirect.com/science/article/pii/S0142727X99000673.

[68] Mohammad Hemmat Esfe, Hadi Hajmohammad, Davood Toghraie, Hadi Rostamian, Omid Mahian, and Somchai Wongwises. Multi-objective optimization of nanofluid flow in double tube heat exchangers for applications in energy systems. *Energy*, 137:160–171, 2017. ISSN 03605442. doi: 10.1016/j.energy.2017.06.104. URL https://doi.org/10.1016/j.energy.2017.06.104.

[69] Didier Astruc. *Transition-metal Nanoparticles in Catalysis: From Historical Background to the State-of-the Art*. 2008. ISBN 9783527315727. doi: 10.1002/9783527621323.ch1.

[70] A. S. Argon and S. Yip. The strongest size. *Philosophical Magazine Letters*, 86(11):713–720, 2006. ISSN 09500839. doi: 10.1080/09500830600986091.

[71] K. Lance Kelly, Eduardo Coronado, Lin Lin Zhao, and George C. Schatz. The optical properties of metal nanoparticles: The influence of size, shape, and dielectric environment. *Journal of Physical Chemistry B*, 107(3):668–677, 2003. ISSN 10895647. doi: 10.1021/jp026731y.

[72] Philipp Reineck, Delia Brick, Paul Mulvaney, and Udo Bach. Plasmonic Hot Electron Solar Cells: The Effect of Nanoparticle Size on Quantum Efficiency. *Journal of Physical Chemistry Letters*, 7(20):4137–4141, 2016. ISSN 19487185. doi: 10.1021/acs.jpclett.6b01884.

[73] Eleonora Petryayeva and Ulrich J. Krull. Localized surface plasmon resonance: Nanostructures, bioassays and biosensing-A review. *Analytica Chimica Acta*, 706(1):8–24, 2011. ISSN 00032670. doi: 10.1016/j.aca.2011.08.020. URL http://dx.doi.org/10.1016/j.aca.2011.08.020.

[74] Claudia Altavilla and Enrico Ciliberto. Inorganic Nanoparticles. 5(October):547, 2011.

[75] Susie Eustis and Mostafa A. El-Sayed. Why gold nanoparticles are more precious than pretty gold: Noble metal surface plasmon resonance and its enhancement of the radiative and nonradiative properties of nanocrystals of different shapes. *Chem. Soc. Rev.*, 35(3):209–217, 2006. ISSN 0306-0012. doi: 10.1039/B514191E. URL http://xlink.rsc.org/?DOI=B514191E.

[76] Prashant K. Jain, Xiaohua Huang, Ivan H. El-Sayed, and Mostafa A. El-Sayed. Review of some interesting surface plasmon resonance-enhanced properties of noble metal nanoparticles and their applications to biosystems. *Plasmonics*, 2(3):107–118, 2007. ISSN 15571955. doi: 10.1007/s11468-007-9031-1.

[77] Sara A. Majetich*, Tianlong Wen, and O. Thompson Mefford*. *Magnetic nanoparticles*, volume 38. 2013. ISBN 9783527627561. doi: 10.1557/mrs.2013.230. URL http://www.journals.cambridge.org/abstract{_}S0883769413002303http://www.journals.cambridge.org/abstract{%}7B{_}{%}7DS0883769413002303.

[78] Abolfazl Akbarzadeh, Mohamad Samiei, and Soodabeh Davaran. Magnetic nanoparticles: preparation, physical properties, and applications in biomedicine. *Nanoscale Research Letters*, 7(1):144, 2012. ISSN 1556-276X. doi: 10.1186/1556-276X-7-144. URL http://nanoscalereslett.springeropen.com/articles/10.1186/1556-276X-7-144.

[79] Bashar Issa, Ihab M. Obaidat, Borhan A. Albiss, and Yousef Haik. Magnetic nanoparticles: Surface effects and properties related to biomedicine applications. *International Journal of Molecular Sciences*, 14(11):21266–21305, 2013. ISSN 16616596. doi: 10.3390/ijms141121266.

[80] Yuping Bao, Tianlong Wen, Anna Cristina S. Samia, Amit Khandhar, and Kannan M. Krishnan. Magnetic nanoparticles: material engineering and emerging applications in lithography and biomedicine. *Journal of Materials Science*, 51(1):513–553, 2015. ISSN 15734803. doi: 10.1007/s10853-015-9324-2.

[81] Program Directors, Charles Ying, Nadia El-masry, and Laverne Hess. *Electronic and Photonic Materials (EPM)*. 2011. ISBN 9783319489315.

[82] A.M. Smith and Shuming Nie. Semiconductor Nanocrystals: Structure, Properties, and Band Gap Engineering. *Acc Chem Res.*, 43(2):190–200, 2010. ISSN 00014842. doi: 10.1021/ar9001069.Semiconductor. URL http://pubs.acs.org/doi/abs/10.1021/ar9001069?ai=53haf=R.